



Satellite-measured water properties in high altitude Lake Tahoe

Menghua Wang^{a,*}, Wei Shi^{a,b}, Shohei Watanabe^c

^a NOAA National Environmental Satellite, Data, and Information Service, Center for Satellite Applications and Research, E/RA3, College Park, MD, USA

^b CIRA at Colorado State University, Fort Collins, CO, USA

^c Tahoe Environmental Research Center, University of California, Davis, CA, USA

ARTICLE INFO

Article history:

Received 20 December 2019

Received in revised form

22 March 2020

Accepted 14 April 2020

Available online 21 April 2020

Keywords:

High-altitude lakes

Lake Tahoe

VIIRS

Satellite ocean color

Normalized water-leaving radiance $nL_w(\lambda)$

Water optical properties

ABSTRACT

It has been difficult in satellite remote sensing to derive accurate water optical, biological, and biogeochemical products over high-altitude inland waters due to issues in satellite data processing (i.e., atmospheric correction). In this study, we demonstrate that accurate normalized water-leaving radiance spectra $nL_w(\lambda)$ can be derived for a high-altitude lake, Lake Tahoe, using improved Rayleigh radiance computations (Wang, M., *Opt. Express*, **24**, 12414–12429, 2016) which accurately account for water surface altitude effects in the Multi-Sensor Level-1 to Level-2 (MSL12) ocean color data processing system. Satellite observations from the Visible Infrared Imaging Radiometer Suite (VIIRS) onboard the Suomi National Polar-orbiting Partnership (SNPP) between 2012 and 2018 are used to evaluate and validate satellite-derived $nL_w(\lambda)$ spectra, and to quantitatively characterize water properties in the lake. Results show that VIIRS-derived $nL_w(\lambda)$ spectra are quite comparable with those from the in situ measurements. Subsequent retrievals of water biological and biogeochemical products show that chlorophyll-a (Chl-a) concentration and Secchi depth (SD) are reasonably well-estimated, and captured normal seasonal variations in the lake, e.g., the annual highest Chl-a and SD normally occur in the winter while the lowest occur in the summer, which is consistent with in situ measurements. Interannual variability of these water quality parameters is also observed. In particular, Lake Tahoe experienced a significant environmental anomaly associated with an extreme weather condition event in 2017, showing considerably decreased $nL_w(\lambda)$ at the spectral bands of 410, 443, and 486 nm, and significantly reduced SD values in the entire lake. The low SD measurements from VIIRS are consistent with in situ observations. Following the event in the 2017–2018 winter, Lake Tahoe recovered and returned to its typical conditions in spring 2018.

Published by Elsevier Ltd.

1. Introduction

Located at an altitude of 1897 m between California and Nevada in the U.S., Lake Tahoe (Fig. 1) is a large fresh water lake and is renowned for its water clarity. It is the second deepest lake (after Crater Lake in southern Oregon) in the U.S. with a length of 35 km, width of 19 km, average depth of 333 m, surface area of about 490 km², and total volume of approximately 156 km³. There are 63 tributaries that provide half of the water supply to Lake Tahoe, which has a drainage area of about the same size as the lake. The evaporation in the region accounts for about two thirds of the total water mass leaving the lake, and the other one third is through the lake's only outlet, the Truckee River.

In the Lake Tahoe region, the climate is characterized by warm dry summers and chilly winters with an average daily maximum temperature of ~25.5 °C in July and an average daily minimum temperature of ~4.6 °C in December. The lake serves as an important resource for the regional economy by attracting tourists from all over the world throughout the year with its winter sports, summer recreations, and other activities and events. Thus, the conservation of lake water quality and the surrounding environment has drawn major political, scientific, and public interest in the region.

Lake Tahoe has a long history of water clarity monitoring using Secchi depth (SD) measurements back to the 1960s (Goldman, 2000; Jassby et al., 1999). In the last five decades, according to the 2018 Tahoe Environmental Research Center report (TERC, 2018), the water clarity in terms of the SD declined consistently from ~30 m in the mid 1960s to ~20 m in recent years (TERC, 2018). The SD decline can be attributed to increased phytoplankton

* Corresponding author.

E-mail address: Menghua.Wang@noaa.gov (M. Wang).

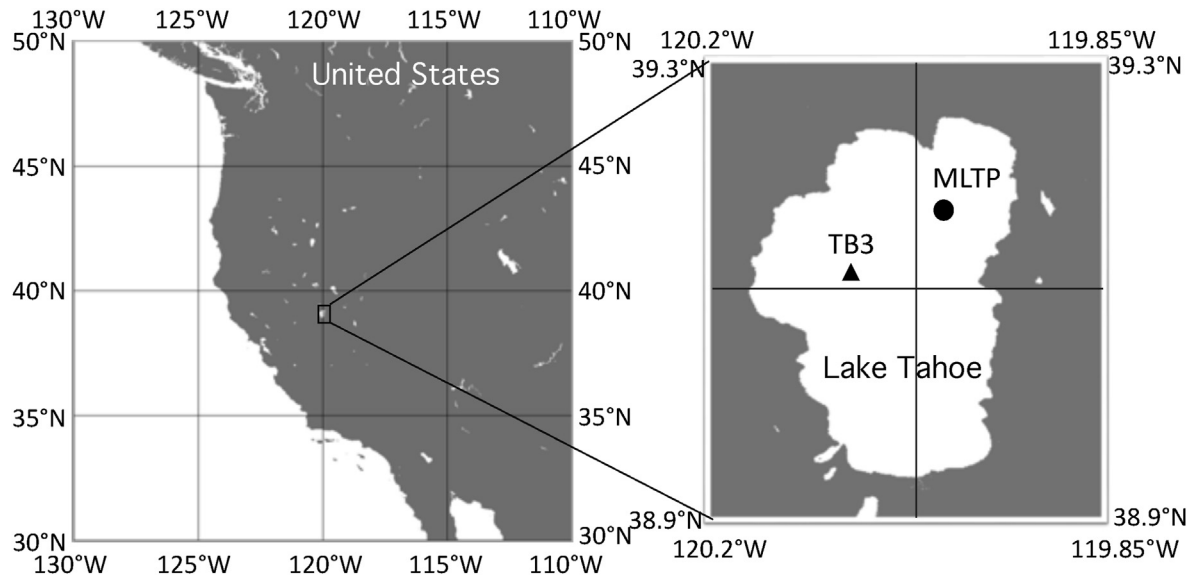


Fig. 1. Map of Lake Tahoe located in California-Nevada of the U.S. The location for the in situ $nL_w(\lambda)$ measurements at the TB3 station [39°06′37″N, 120°04′31″W] and in situ Chl-a and SD at the MLTP station [39°8′30″ N 120°00′55.5″W] are also marked.

concentration and the amount of fine sediment particles in the lake (Jassby et al., 1999, 2003). Seasonally, one of the SD minimums occurs in June due to increased suspended sediment discharges with the melting of snowpack, and another SD minimum occurs in December primarily as a result of mixed-layer deepening (Jassby et al., 1999). The long-term SD model also shows that the interannual variability of SD in the lake can be driven by weather changes such as precipitation anomalies in the region (Jassby et al., 2003).

In addition, Lake Tahoe shows a long-term warming trend due to the upward trend of air temperature and incoming longwave radiation in the region (Coats et al., 2006). Indeed, the volume-weighted mean temperature increased about 0.015 °C/year between 1970 and 2002. The thermal structure of the lake also shows changes, e.g., the decreasing depth of the thermocline and the increase of resistance of the water in the lake to vertical layer mixing and stratification (Coats et al., 2006; Sahoo et al., 2016). In Lake Tahoe, both upwelling and surface circulation are observed and characterized with satellite remote sensing from the Advanced Spaceborne Thermal Emission and Reflection Radiometer (ASTER) (Hook et al., 2007; Tonooka and Palluconi, 2005; Tonooka et al., 2005), the Landsat Enhanced Thematic Mapper (ETM) (Barsi et al., 2007; Hook et al., 2004), and the Moderate Resolution Imaging Spectroradiometer (MODIS) (Hook et al., 2007). The upwelling of the intermediate-depth water was observed to occur frequently in the spring and summer seasons. It brings the water from the depth of ~10–30 m to the surface, and leads to enhanced phytoplankton growth and decreased water clarity in Lake Tahoe (Steissberg et al., 2005).

As one of the main drivers of the water clarity trend in Lake Tahoe, the rate of phytoplankton growth has been steadily increasing over the past 50 years. Indeed, primary productivity increased from < ~50 g C m⁻² year⁻¹ in 1959 to > ~200 g C m⁻² year⁻¹ in recent years (TERC, 2018). In addition, the aerosol deposition provides most of the nutrients in the dissolved inorganic particles and total nitrogen, as well as a significant amount of the total phosphorus loading in Lake Tahoe (Jassby et al., 1994). In fact, the annual nitrogen (N), phosphorous (P), and particulate matter (PM) from the aerosol deposition in the lake are estimated to be about 185, 3, and 755 metric tons (Dolislager et al., 2012), respectively. Indeed, these nutrients from the aerosol deposition

contributed to the long-term increase of Chl-a concentration, water primary productivity, and biomass in Lake Tahoe (Mackey et al., 2013). Specifically, it has been found that the phytoplankton amount in Lake Tahoe is becoming phosphorus-limited from the nitrogen-limited because the deposited aerosols in the lake contain nutrients with high N:P ratios (Chang et al., 1992; Mackey et al., 2013). However, it is noted that, in addition to the phosphorous limitation, phytoplankton growth in Lake Tahoe is also iron-limited (Chang et al., 1992).

In situ water optics measurements have long been conducted to characterize and quantify optical and bio-optical properties in Lake Tahoe. The spectral irradiance and beam transmittance were measured as a function of water depth in the lake (Smith et al., 1973). A blue color index was also developed using the remote sensing reflectance $R_{rs}(\lambda)$ measurements to quantitatively analyze the spatial and seasonal variations (Watanabe et al., 2016). It is noted that the remote sensing reflectance $R_{rs}(\lambda)$ (as a function of the wavelength λ) is defined as $R_{rs}(\lambda) = nL_w(\lambda)/F_0(\lambda)$, where $nL_w(\lambda)$ and $F_0(\lambda)$ are the normalized water-leaving radiance (Gordon, 2005; Morel and Gentili, 1996; Wang, 2006) and the mean extraterrestrial solar irradiance (Thuillier et al., 2003), respectively. As an oligotrophic subalpine lake, the role of ultraviolet (UV) radiation, and the patterns of spatial and temporal variability of UV transparency were investigated (Rose et al., 2009). It was found that UV transparency differs from the photosynthetically available radiation (PAR). In fact, the combination of the UV and visible water transparency can provide a more comprehensive understanding of the ecosystem changes and the biological and biogeochemical processes in Lake Tahoe (Rose et al., 2009).

Satellite observations over global inland waters can provide an effective tool to monitor the lake environmental changes such as algae bloom and water clarity. Using the shortwave infrared (SWIR)-based atmospheric correction algorithm (Wang, 2007; Wang and Shi, 2005, 2007; Wang et al., 2009b), it has been demonstrated that MODIS-derived water optical property data, e.g., $nL_w(\lambda)$ spectra, can be used to monitor and assess water property (quality) in turbid Lake Taihu in China (Wang et al., 2011). The spatial and temporal water turbidity variations in Lake Okeechobee are also characterized using MODIS measurements (Wang et al., 2012a). Furthermore, the cyanobacteria blooms in Lake Taihu are

quantitatively assessed and evaluated from MODIS observations (Hu et al., 2010). In addition to water optical parameters such as $nL_w(\lambda)$ spectra, lake surface temperature and many other water quality parameters, such as the water diffuse attenuation coefficient at 490 nm $K_d(490)$ (Lee et al., 2005; Wang et al., 2009a), Chl-a concentrations (Hu et al., 2012; O'Reilly et al., 1998; O'Reilly and Werdell, 2019; Wang and Son, 2016), total suspended matter (TSM) (or suspended particulate matter (SPM)) concentrations (Knaeps et al., 2015; Nechad et al., 2010; Shi et al., 2018; Yu et al., 2019), SD (Binding et al., 2015; Lee et al., 2016), float algae index (Hu, 2009), and inherent optical properties (IOPs) (Lee et al., 2002; Shi et al., 2019; Werdell et al., 2013), can also be routinely and reliably derived from satellite remote sensing observations. These satellite water quality property data can be further used to study global lakes to characterize and quantify the long-term water physical, optical, biological, and biogeochemical variability (Bolgrien and Brooks, 1992; Shi and Wang, 2015; Shi et al., 2018; Son and Wang, 2019). In all of these studies, however, satellite reflective solar radiance data (water color) are applied almost all to global around sea-level inland waters.

Lake Tahoe has long been used as one of the sites for validation of the absolute radiometric calibration and surface geophysical products derived from various satellite sensors (mostly for thermal bands and their corresponding applications) such as ASTER, MODIS, Landsat 5 and ETM+ (Barsi et al., 2007; Hook et al., 2007; Steissberg et al., 2005; Tonooka and Palluconi, 2005; Tonooka et al., 2005), as well as for the sensor preflight and in-flight calibration (Parada et al., 1997; Thome et al., 1998). However, few satellite reflective solar radiance observations have ever been used to characterize and quantify the lake ecosystem, and monitor water optical, biological, and biogeochemical changes. This is mainly due to issues in the satellite data processing, i.e., atmospheric correction (Gordon and Wang, 1994; IOCCG, 2010; Wang, 2007), to accurately account for the effect of lake surface altitude (Wang, 2016). Specifically, the top-of-atmosphere (TOA) Rayleigh scattering radiance computations were incorrect for high-altitude lakes (Wang, 2016), leading to over-subtraction of the TOA Rayleigh-scattering radiance contributions, and thereby deriving biased low $nL_w(\lambda)$ spectra (often negative values depending on the lake surface altitude) (Gordon and Wang, 1994; Wang, 2016). Consequently, satellite-derived optical, biological, and biogeochemical products (e.g., Chl-a, $K_d(490)$, SD, IOPs, or any other products that use the inputs of satellite-measured $nL_w(\lambda)$ spectra) for global high-altitude lakes were in error, and generally cannot be used. This includes satellite-derived water quality products over global high-altitude lakes from the Sea-viewing Wide-field-of-view Sensor (SeaWiFS), MODIS, and the Visible Infrared Imaging Radiometer Suite (VIIRS), etc. It is noted that for global ocean color data processing the required ancillary data such as sea-level atmospheric pressure, total column ozone amount, sea surface wind speed, and total column water-vapor amount are routinely obtained from the National Center for Environmental Prediction (NCEP) (Ramachandran and Wang, 2011).

Following a recent effort for improving the TOA Rayleigh radiance computations for satellite ocean/water color remote sensing, in particular, for accounting for the water surface altitude effect (Wang, 2016), the global VIIRS observations on both the Suomi National Polar-orbiting Partnership (SNPP) and NOAA-20 satellites are processed using the improved Rayleigh radiance computations in the Multi-Sensor Level-1 to Level-2 (MSL12) ocean color data processing system (Wang et al., 2013). In this study, we use Lake Tahoe as an example to demonstrate that high quality $nL_w(\lambda)$ spectra can now be derived from VIIRS measurements for global high-altitude lakes to characterize and quantify the lake ecosystem as well as monitor environmental changes. Specifically, VIIRS-SNPP-derived $nL_w(\lambda)$ spectra are compared with those from the in

situ measurements and shown to have good results. Furthermore, based on the in situ SD measurements in the lake, a regional empirical SD algorithm has been developed using the VIIRS-derived $nL_w(\lambda)$ at the wavelength of 551 nm. Therefore, the seasonal and interannual variabilities of $nL_w(\lambda)$, Chl-a, and SD in Lake Tahoe are characterized and quantified. In particular, we show that when using VIIRS-derived water property data the anomalous water property in Lake Tahoe during the 2017–2018 abnormal event can be quantitatively investigated and analyzed. Finally, the potential to use Lake Tahoe as an ocean color validation site for evaluation and validation of satellite ocean color products, as well as routine sensor performance monitoring (Wang et al., 2015), is discussed.

2. Satellite-derived and in situ-measured water properties in Lake Tahoe

2.1. VIIRS-measured $nL_w(\lambda)$ spectra and other water color products

Successfully launched in October 2011, VIIRS-SNPP provides continuous observations of the Earth's atmosphere, land, cryosphere, and ocean properties with the 14 reflective solar bands (RSBs) covering a spectral range of 410–2257 nm (Goldberg et al., 2013). For the satellite ocean and inland water color remote sensing, the VIIRS-SNPP five visible bands (M1–M5) at the nominal central wavelengths of 410, 443, 486, 551, and 671 nm, two imaging (I) bands (I1 and I2) at 638 and 862 nm, two near-infrared (NIR) bands (M6 and M7) at 745 and 862 nm, and three SWIR bands (M8, M10, and M11) at 1238, 1601, and 2257 nm are used to derive VIIRS $nL_w(\lambda)$ spectra over the global ocean and coastal/inland waters (Wang and Jiang, 2018b; Wang et al., 2013). It is noted that VIIRS measurements have spatial resolutions of 750 m and 375 m for the M-bands and I-bands, respectively. Thus, VIIRS-derived $nL_w(\lambda)$ spectra at the spatial resolution of 750 m are applicable for global open oceans (Wang et al., 2016a), while $nL_w(\lambda)$ at the image bands (e.g., $nL_w(638)$ data) with the spatial resolution of 375 m are useful for various coastal and inland water applications (Wang and Jiang, 2018b).

VIIRS global ocean and inland water color products have been routinely generated since 2012 using MSL12, which was originally developed for producing consistent global ocean color data sets from multiple satellite sensors using a common data processing software (Wang, 1999; Wang et al., 2002). It should be noted that for deriving accurate global ocean color products the on-orbit vicarious calibration has been carried out for VIIRS using the in situ MOBY measurements (Clark et al., 1997) in the waters off Hawaii (Wang et al., 2016b). During the VIIRS period, MSL12 has been significantly modified and improved, including an atmospheric correction algorithm (Jiang and Wang, 2014; Wang and Jiang, 2018a; Wang et al., 2012b), cloud masking using the SWIR bands (Wang and Shi, 2006), straylight and cloud shadowing detection (including the adjacency effect) (Bulgarelli et al., 2017; Hu et al., 2020; Jiang and Wang, 2013), as well as improved satellite algorithms for various ocean/water color products, e.g., Chl-a (Wang and Son, 2016), $K_d(490)$ (Wang et al., 2009a), IOPs (Shi and Wang, 2019), data quality assurance (QA) (Wei et al., 2016), etc. In particular, improved TOA Rayleigh radiance computations for accurately accounting for the effects of high-altitude inland waters have been developed and implemented in MSL12 (Wang, 2016). It should be noted that in the MSL12 ocean/water color data processing the atmospheric diffuse transmittance (IOCCG, 2010; Yang and Gordon, 1997) has also been modified to account for the high-altitude lake surface atmospheric pressure changes (i.e., accounting for the Rayleigh optical thickness variations) for both the solar and viewing directions. This is also an important fact impacted directly by the Rayleigh optical thickness variation due to

significant atmospheric pressure changes over high-altitude lakes (IOCCG, 2010). However, it is assumed that there is negligible change in the Rayleigh-aerosol interaction radiance term (Gordon and Wang, 1994; IOCCG, 2010; Wang, 2007) in the VIIRS data processing for a high-altitude lake. It should also be noted that VIIRS-derived ocean color products have been well evaluated and validated over various ocean regions and some sea-level inland waters through presentations in various conferences, meetings, and workshops, as well as publications (Barnes et al., 2019; Hlaing et al., 2013; Mikelsons et al., 2020; Wang et al., 2016a). However, VIIRS-derived inland water quality products have not been evaluated over any high-altitude lakes such as Lake Tahoe.

One of the important issues for deriving accurate water property data over high-altitude inland waters from remote sensing is to accurately account for the water surface altitude effect in the TOA Rayleigh radiance computations (Wang, 2016), in addition to various other challenges related to the data processing over global sea-level waters. This problem existed in previous satellite ocean color data processing, which assumed the sea-level water surface property (i.e., atmospheric pressure measured and used at the sea-level) (Gordon et al., 1988a; Wang, 2002, 2005). For high-altitude lakes such as Lake Tahoe, this leads to an over-estimation of the TOA spectral Rayleigh radiance contributions (therefore, over subtractions of Rayleigh radiance values in atmospheric correction), thereby deriving biased low $nL_w(\lambda)$ spectra (or even negative values) (Gordon and Wang, 1994; IOCCG, 2010; Wang, 2007). For example, the ratio of the surface atmospheric pressure at 2 km altitude to that at sea-level is about 0.78, i.e., the TOA Rayleigh-scattering radiance values over a 2 km altitude lake have an approximately similar factor smaller than those over the sea-level lakes (Wang, 2016).

In fact, for high-altitude inland waters, the accurate calculation of the TOA spectral Rayleigh scattering radiances is really important (particularly for the short visible bands) because the TOA radiances contributed from aerosols are usually less important because aerosols are mostly located close to sea-level (e.g., within ~2 km). With the improved TOA Rayleigh radiance computation in MSL12 (Wang, 2016), the effects of high-altitude lakes (i.e., significantly low atmospheric pressure, and therefore, reduced spectral Rayleigh optical thicknesses) are accurately accounted for. Therefore, water property data can be derived accurately over global high-altitude waters including Lake Tahoe.

2.2. In situ-measured $nL_w(\lambda)$ spectra

As NASA's calibration site, four permanent moored buoys located at different locations in Lake Tahoe routinely make in situ measurements such as longwave and shortwave radiations, wind speed and direction, atmospheric pressure, aerosol optical depth (AOD), and water skin temperature (<https://laketahoe.jpl.nasa.gov/measurements>). Specifically, the moored buoy at the TB3 station as noted in Fig. 1 is located at [39°06'37"N, 120°04'31"W]. Hyperspectral radiance measurements in the wavelength range of 360 nm–875 nm were taken with the hyperspectral radiometers installed at above water surface (0^+ m), 2 m, and 9 m depths on the TB3 buoy. Each radiometer measured the downward spectral irradiance $E_d(\lambda, z)$ and upward spectral radiance $L_u(\lambda, z)$ as a function of water depth z . Measurements were made hourly from local time 6:00 to 19:00. The water attenuation coefficient for $L_u(\lambda, z)$ was then calculated, and consequently, $L_u(\lambda, 0^+)$ (calculated from $L_u(\lambda, 0^-)$) was estimated. Finally, the remote sensing reflectance spectra $R_{rs}(\lambda)$ were calculated with $L_u(\lambda, 0^+)$ and $E_d(\lambda, 0^+)$ (Watanabe et al., 2016).

During 2013, in situ in-water radiometric profile data were also taken at the TB3 station and mid-lake stations with another vertical profiling hyperspectral radiometer system within 2 h of the local

solar noon on March 1, April 28, July 25, September 9, October 25, and December 16. Remote sensing reflectance spectra $R_{rs}(\lambda)$ were then calculated from the measurements of the subsurface upward spectral radiance $L_u(\lambda, 0^-)$ and the downward spectral irradiance $E_d(\lambda, 0^+)$ (Watanabe et al., 2016).

A total of 14 in situ $R_{rs}(\lambda)$ spectra measurements as described above at the station TB3 in the lake were shown in Watanabe et al. (2016). Specifically, these in situ $R_{rs}(\lambda)$ spectra covered a time period from December 16, 2013, to April 15, 2015. In this study, these 14 in situ $R_{rs}(\lambda)$ spectra acquired at the TB3 station in Lake Tahoe (Fig. 1) were converted to in situ $nL_w(\lambda)$ spectra to further compare, evaluate, and validate VIIRS-derived $nL_w(\lambda)$ spectra.

In addition to the in situ radiometric measurements at the TB3 station, continuous water quality monitoring has been routinely conducted since 1968. The SD and Chl-a (at the depths of 0, 10, 50, 100 m) have been sampled routinely approximately every 34 days at the Mid-Lake Tahoe Productivity (MLTP) station located at [39°8'30"N, 120°00'55.5"W] (noted in Fig. 1). The in situ SD measurements and coincident VIIRS-derived $nL_w(\lambda)$ at the green band (551 nm) can be used to develop an empirical algorithm to derive SD (Binding et al., 2008). The temporal variations of VIIRS-derived Chl-a and SD data at the MLTP station are compared with those from the in situ measurements to evaluate satellite algorithms performance for these two important water property products.

3. Results

3.1. VIIRS-derived $nL_w(\lambda)$ spectra compared with those from in situ measurements

There are 10 (out of 14) radiance matchups for VIIRS-SNPP-derived and in situ-measured $nL_w(\lambda)$ spectra at the TB3 station on the same date in Lake Tahoe. To compare the VIIRS-SNPP-derived and in situ-measured $nL_w(\lambda)$, a box of 7×7 pixels (remapped with a box about 1×1 km²) centered at the TB3 station in the remapped $nL_w(\lambda)$ image was set, and the median of $nL_w(\lambda)$ values in the box was calculated as the VIIRS-derived $nL_w(\lambda)$ value in order to compare with the in situ $nL_w(\lambda)$ spectra. There were four cases with the cloud cover when VIIRS-SNPP passed over the TB3 station, preventing the production of valid VIIRS $nL_w(\lambda)$ spectra. Fig. 2 provides examples of comparative results between VIIRS-derived and in situ-measured $nL_w(\lambda)$ spectra at the TB3 station on June 15, 2013 (Fig. 2a), July 15, 2013 (Fig. 2b), August 15, 2013 (Fig. 2c), and September 15, 2013 (Fig. 2d). The comparisons in Fig. 2 show that VIIRS-derived $nL_w(\lambda)$ spectra match quite well with those from the in situ measurements, and the two data sets are generally consistent (Fig. 2). However, there are some minor differences in the matchups in $nL_w(\lambda)$ as VIIRS-derived $nL_w(410)$ and $nL_w(443)$ are slightly biased low on June 15, 2013, relative to those from the in situ measurements. Overall, results in Fig. 2 demonstrate that VIIRS-derived $nL_w(\lambda)$ spectra using the improved new Rayleigh radiance computation in MSL12 are generally accurate, showing significant improvements compared to those with incorrect Rayleigh radiance computations for global high-altitude lakes (i.e., significantly biased low $nL_w(\lambda)$ values, and even negative at the blue bands).

The overall accuracy of VIIRS-derived $nL_w(\lambda)$ spectra at the TB3 station is further evaluated (Fig. 3). Since Lake Tahoe has high water clarity, values of $nL_w(638)$ and $nL_w(671)$ are generally very small (close to zero). Differences in matchups for $nL_w(638)$ and $nL_w(671)$ are significantly amplified in the logarithmic scale as shown in Fig. 3, although the differences are actually trivial. For $nL_w(\lambda)$ at the blue and green bands (wavelengths at 410, 443, 486, and 551 nm), VIIRS-derived $nL_w(\lambda)$ data agree quite well with the in situ measurements, with the mean $nL_w(\lambda)$ ratio value between VIIRS-

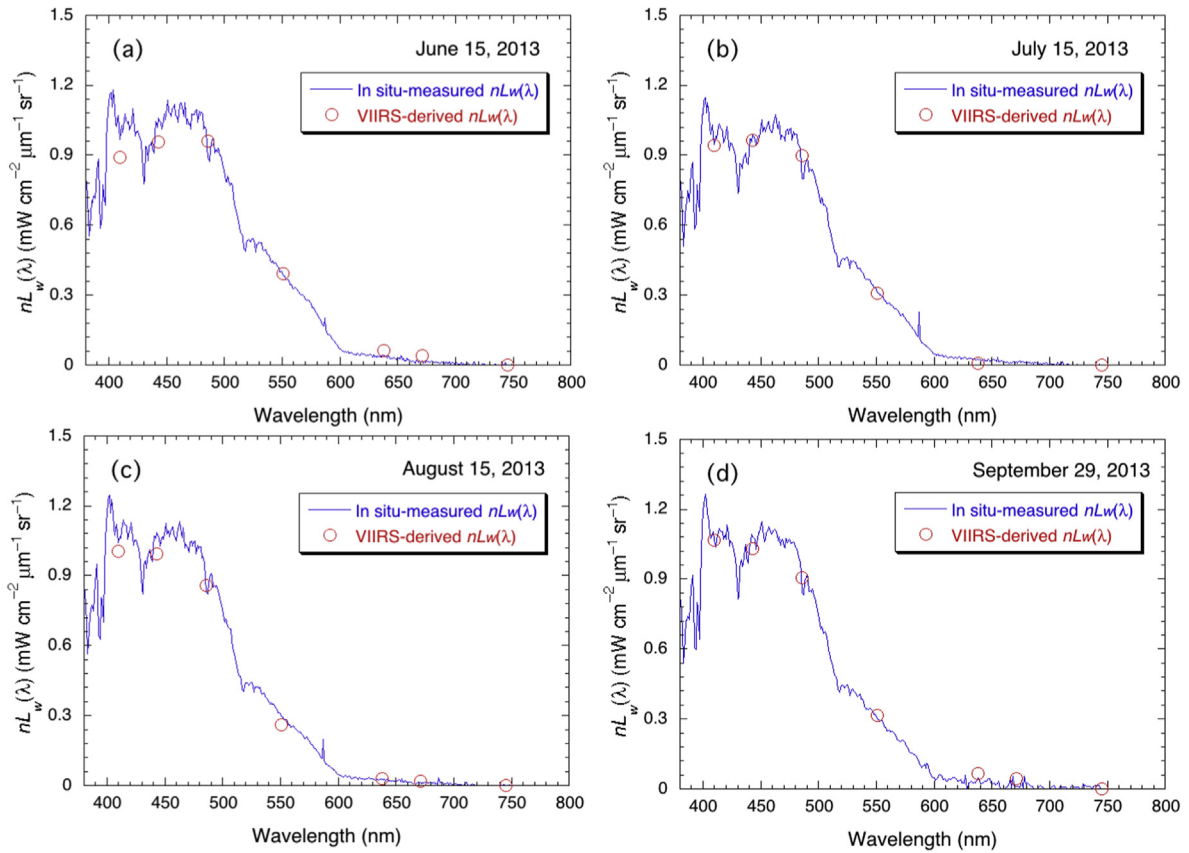


Fig. 2. (a) Comparisons of VIIRS-SNPP-derived and in situ-measured $nL_w(\lambda)$ spectra at the TB3 station in Lake Tahoe for the measurement dates of (a) June 15, 2013, (b) July 15, 2013, (c) August 15, 2013, and (d) September 29, 2013.

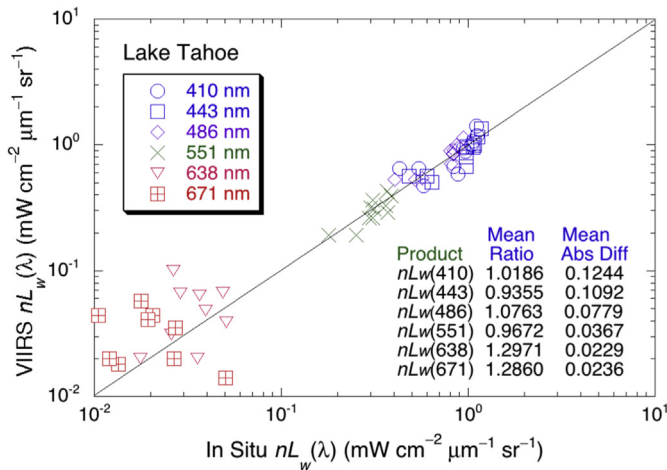


Fig. 3. Scatter plot of VIIRS-SNPP-derived $nL_w(\lambda)$ versus in situ-measured $nL_w(\lambda)$ at the VIIRS spectral bands of 410, 443, 486, 551, 638, and 671 nm. Values of mean ratio (Mean Ratio, unitless) and mean absolute difference (Mean Abs Diff, unit of $mW\ cm^{-2}\ \mu m^{-1}\ sr^{-1}$) between VIIRS-derived and in situ-measured $nL_w(\lambda)$ at the six VIIRS spectral bands are also indicated in the plot.

derived and in situ-measured $nL_w(\lambda)$ of 0.999 and the coefficient of determination R^2 between the two data sets (in linear scale) of 0.857. Specifically, the mean $nL_w(\lambda)$ ratio values between VIIRS-derived and in situ-measured $nL_w(\lambda)$ at the VIIRS wavelengths of 410, 443, 486, 551, 638, and 671 nm are 1.019, 0.936, 1.076, 0.967, 1.297, and 1.286, respectively, while the mean $nL_w(\lambda)$ absolute

difference values between the two for the corresponding six VIIRS bands are 0.124, 0.109, 0.078, 0.037, 0.023, and 0.024 $mW\ cm^{-2}\ \mu m^{-1}\ sr^{-1}$, respectively. It should be noted again that, for small values such as $nL_w(\lambda)$ at the VIIRS red bands (638 and 671 nm), the mean absolute difference is a better and more meaningful measure for describing the uncertainty. In fact, it shows the smallest mean absolute difference values for $nL_w(\lambda)$ at the red bands although the $nL_w(\lambda)$ ratios at these bands are the largest due to very small values. Results in Figs. 2 and 3 confirm that high-quality $nL_w(\lambda)$ spectra can be derived from VIIRS-SNPP observations over Lake Tahoe. Therefore, the lake water optical, biological, and biogeochemical property data (e.g., Chl-a and SD) can be derived from VIIRS-SNPP-measured $nL_w(\lambda)$ spectra, and these data can be used to study the lake water property dynamics, characterize and quantify the long-term ecosystem variability, monitor environmental change, and detect hazardous events over the global high-altitude lakes. These possibilities and potentials are evaluated and discussed below.

3.2. VIIRS-derived SD and Chl-a compared with the in situ data

In Lake Tahoe, the SD variations are correlated to the amount of fine sediment in the water column (Jassby et al., 1999, 2003). Loading and settling rates of such fine inorganic particles (<~16 μm in diameter) were found to have the largest impact on the lake clarity (Sahoo et al., 2010). Considering the fact that $nL_w(\lambda)$ at the red end of the spectrum (638 and 671 nm) are usually close to zero for the lake, $nL_w(551)$ can be a sensitive indicator for the inorganic particle concentrations and correlate with water clarity. Indeed, Binding et al. (2015) showed that the SD in the Great Lakes can be well correlated to satellite-derived $nL_w(551)$ values. At the MLTP

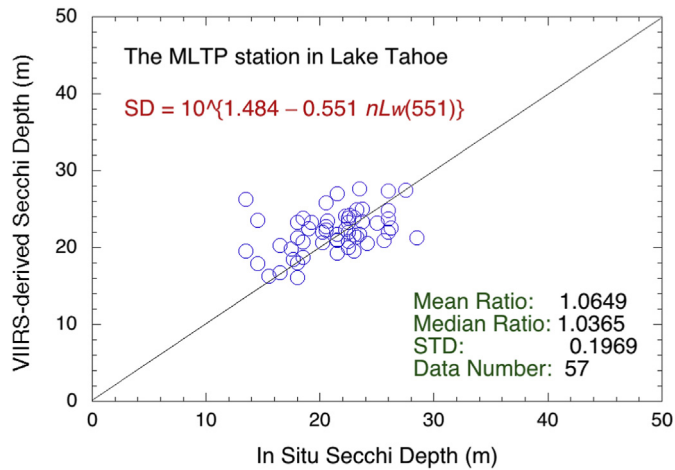


Fig. 4. VIIRS-derived SD compared with those from the in situ measurements at the MLTP station in Lake Tahoe.

station in Lake Tahoe (Fig. 1), there are total of 57 valid VIIRS $nL_w(\lambda)$ retrievals coincident with the in situ SD measurements in the period between 2012 and 2018. Using these 57 sets of data, an empirical SD model for the lake can then be developed and described as following:

$$SD = 10^{(a_0 + a_1 \times nL_w(551))} \quad (1)$$

where coefficients $a_0 = 1.484$ and $a_1 = -0.551 \text{ mW}^{-1} \text{ cm}^2 \mu\text{m sr}$, which were derived from the best fit to the in situ SD data to VIIRS-derived $nL_w(551)$. Fig. 4 shows a comparison between the VIIRS-derived (using Eq. (1)) and in situ-measured SD at the MLTP station. The mean and median ratios of the VIIRS-derived SD and in situ values are 1.0649 and 1.0365 with the standard deviation (STD) of 0.1969. The comparison results (Fig. 4) show that VIIRS-derived SD data are quite reasonable and can be used to estimate water clarity in the lake from satellite observations.

Fig. 5 further provides the performance evaluation of VIIRS-derived Chl-a (Fig. 5a) and SD (Fig. 5b) with the corresponding in situ measurements at the MLTP station during the period of 2012–2018. VIIRS-derived Chl-a data show the same seasonal trend as that from the in situ Chl-a measurements, i.e., high Chl-a in the winter and low Chl-a in the summer. It should be noted that in situ Chl-a data were derived as mean values from measured Chl-a data at the surface and at 10 m water depth, considering SD values are normally between 20 and 30 m (therefore, excluding in situ Chl-a data at 50 and 100 m). Results show that VIIRS-derived low Chl-a values in the MLTP station are $\sim 0.2 \text{ mg m}^{-3}$ and consistent with those from in situ data. However, some discrepancies between VIIRS-derived and in situ-measured Chl-a can be found for high Chl-a values in the winter season. For example, VIIRS-derived Chl-a had the same peaks as the in situ measurements in the winters of 2012–2013, 2013–2014, and 2017–2018. VIIRS-derived Chl-a was particularly different from the in situ data in the winter of 2016–2017 (Fig. 5a).

VIIRS-derived SD data in the MLTP station show the same seasonal and interannual variations as those from the in situ SD measurements (Fig. 5b). In the period between 2012 and 2016, VIIRS-derived SD data were consistent with the in situ measurements in terms of both the magnitude and seasonal variation. However, relatively large SD discrepancies between them were found with anomalously low in situ SD measurements in mid-2016 and late 2017, although the SD seasonal variation from the two SD data sets was still the same.

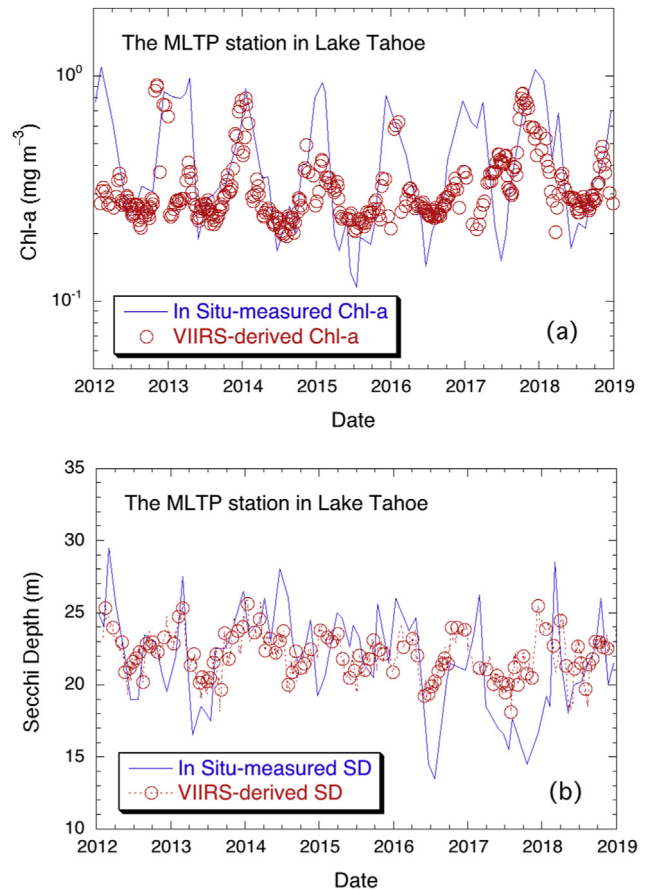


Fig. 5. VIIRS-derived water quality products compared with those from the in situ measurements at the MLTP station between 2012 and 2018 for (a) Chl-a and (b) SD. Note that in situ Chl-a data were derived with the mean from measured Chl-a values at the surface and 10 m water depth.

Although there are some disagreements in the magnitude for VIIRS and in situ measured SD (Figs. 4 and 5b) and Chl-a (Fig. 5a), results are generally consistent in terms of magnitude values and particularly in their variations. It should be noted that the in situ SD and Chl-a measurements also have their own uncertainties due to the instrument limitations and the operation differences, e.g., human factors for the SD estimation. These uncertainties also contribute to the differences between VIIRS and in situ measured Chl-a and SD data. Therefore, we can conclude that VIIRS-derived Chl-a and SD data have reasonably good accuracy, and these data products along with VIIRS-derived $nL_w(\lambda)$ spectra can be used to study water properties in Lake Tahoe.

3.3. VIIRS-measured climatology of $nL_w(\lambda)$, Chl-a, and SD

Noticeably, there are some significant differences in VIIRS-derived water property data in 2017 and early 2018, compared with those in the other years. Indeed, an anomalous event happened in the period of 2017 to early 2018 in the region, and significantly impacted water properties in Lake Tahoe (Staff-Report, 2018). Therefore, for the calculations of climatology water properties in the lake, VIIRS measurements from 2012 to 2016 (excluding years 2017 and 2018) are used.

Fig. 6 provides the climatology images of $nL_w(410)$ (Fig. 6a), $nL_w(443)$ (Fig. 6b), $nL_w(486)$ (Fig. 6c), $nL_w(551)$ (Fig. 6d), $nL_w(638)$ (Fig. 6e), $nL_w(671)$ (Fig. 6f), Chl-a (Fig. 6g), and SD (Fig. 6h), which were calculated as the median of all valid retrievals from VIIRS-

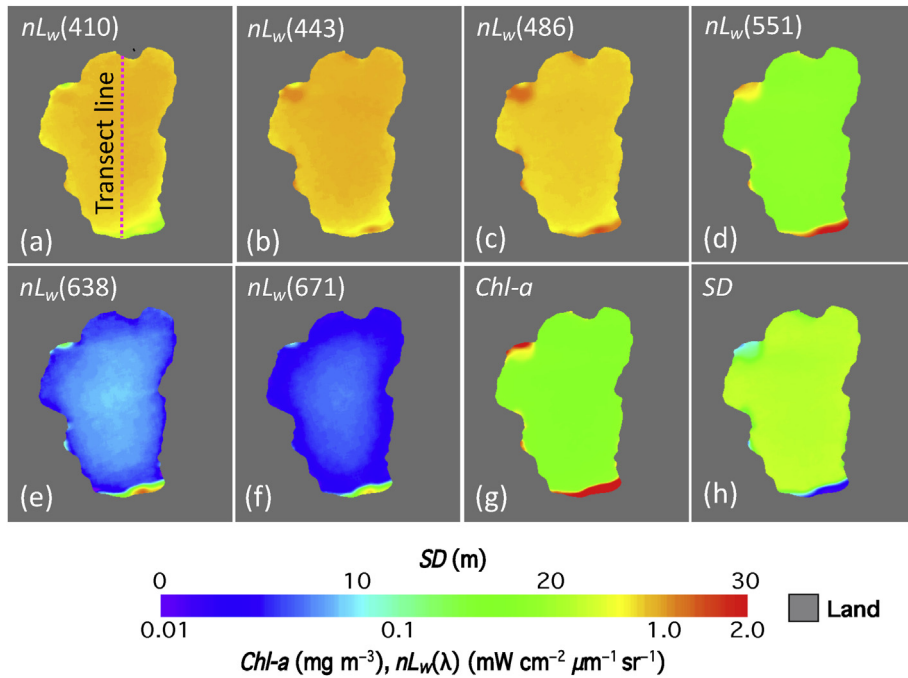


Fig. 6. VIIRS-derived climatology (2012–2016) water property data in Lake Tahoe for (a) $nL_w(410)$, (b) $nL_w(443)$, (c) $nL_w(486)$, (d) $nL_w(551)$, (e) $nL_w(638)$, (f) $nL_w(671)$, (g) Chl-a, and (h) SD. The transection line in panel (a) from the north to south at 120.02°W is marked for further data analysis.

SNPP measurements between 2012 and 2016, providing the normal water optical, biological, and biogeochemical conditions of the lake. Results from VIIRS observations show that Lake Tahoe features spatial uniformity in water properties and enhanced $nL_w(\lambda)$ at the blue bands, except for small areas in the southern and northwestern parts of the lake where water depth is less than ~20 m. Fig. 6 shows that spatial distributions of Chl-a, SD, and $nL_w(\lambda)$ in the lake are quite uniform and there is little spatial difference with normal Chl-a $\sim 0.25 \text{ mg m}^{-3}$ and SD $\sim 22 \text{ m}$ for the entire lake. The changes of $nL_w(\lambda)$ spectra are also small across the lake for $nL_w(\lambda)$ at the all VIIRS bands. In fact, there is no specific spatial pattern for all climatology $nL_w(\lambda)$ spectra in the lake. Spectrally, VIIRS-derived $nL_w(\lambda)$ spectra show the typical feature of clear blue waters (Gordon et al., 1988b; Morel and Maritorena, 2001), showing $nL_w(443)$ (Fig. 6b) $\sim 0.8 \text{ mW cm}^{-2} \mu\text{m}^{-1} \text{ sr}^{-1}$, while $nL_w(410)$ (Fig. 6a) and $nL_w(486)$ (Fig. 6c) are a little bit less than $nL_w(443)$. In comparison, the climatology $nL_w(551)$ (Fig. 6d) in the lake is $\sim 0.3 \text{ mW cm}^{-2} \mu\text{m}^{-1} \text{ sr}^{-1}$. Both $nL_w(638)$ (Fig. 6e) and $nL_w(671)$ (Fig. 6f) are less than $\sim 0.05 \text{ mW cm}^{-2} \mu\text{m}^{-1} \text{ sr}^{-1}$.

A transect line from the north to south across the lake is defined to further characterize the uniformity of the lake spatial distributions in $nL_w(\lambda)$ spectra, Chl-a, and SD (Fig. 6a). Fig. 7 provides quantitative results of $nL_w(\lambda)$ spectra, Chl-a, and SD as a function of distance from the north to south along the transect line noted in Fig. 6a. Fig. 7a shows that climatology $nL_w(443)$ is generally stable at $\sim 0.8 \text{ mW cm}^{-2} \mu\text{m}^{-1} \text{ sr}^{-1}$ from the north of the transect line to 20 km in the lake, and it trends a little lower to $\sim 0.6 \text{ mW cm}^{-2} \mu\text{m}^{-1} \text{ sr}^{-1}$ from 20 km to 30 km. However, climatology $nL_w(551)$ value ($\sim 0.3 \text{ mW cm}^{-2} \mu\text{m}^{-1} \text{ sr}^{-1}$) is quite stable and does not show any noticeable change along the transect line (Fig. 7a). In the southern end of the transect line, the water type changes from a typical clear blue water to a typical shallow (bottom-affected) water with significantly enhanced $nL_w(\lambda)$ in the visible bands (Fig. 7a).

The variations of climatology Chl-a and SD along the transect line are shown in Fig. 7b. Chl-a shows little variation with a value of $\sim 0.25 \text{ mg m}^{-3}$ for the majority of the lake even though it increases

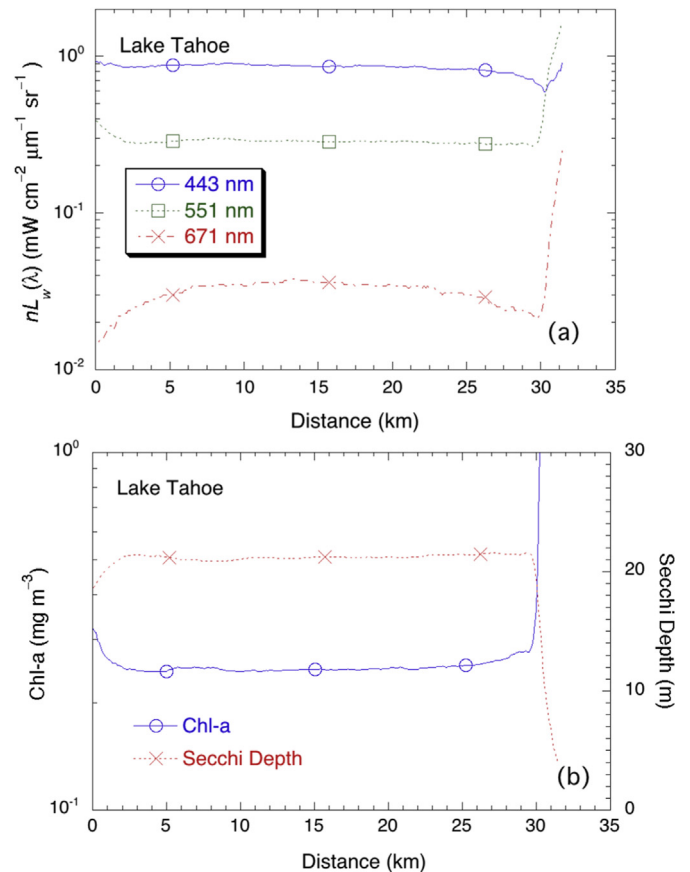


Fig. 7. VIIRS-derived climatology (2012–2016) water property data along the transection line (noted in Fig. 6a) in Lake Tahoe for products of (a) $nL_w(443)$, $nL_w(551)$, and $nL_w(671)$ and (b) Chl-a and SD.

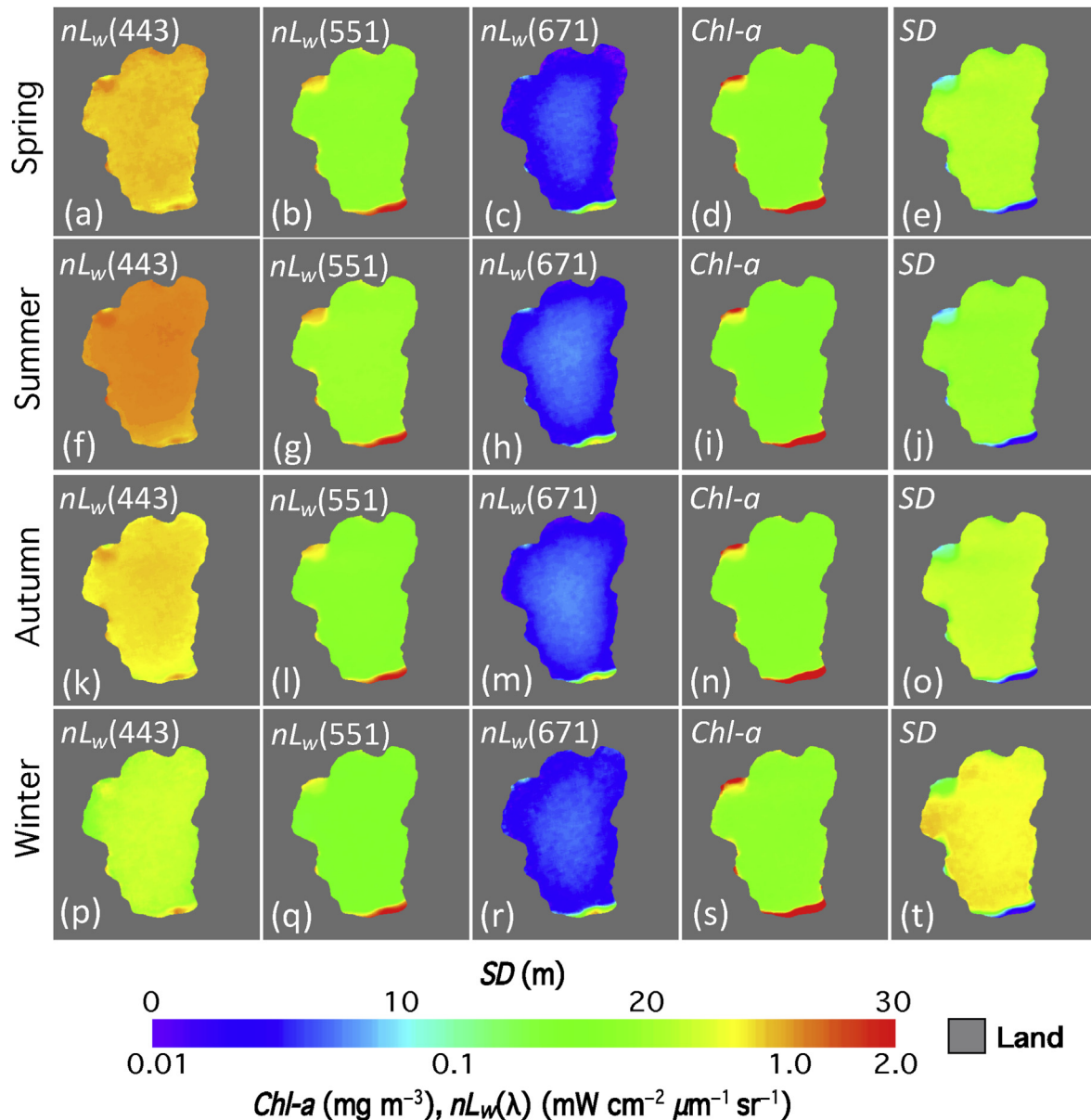


Fig. 8. VIIRS-derived seasonal maps of water properties (2012–2016) in Lake Tahoe for products of (along the row) $nL_w(443)$, $nL_w(551)$, $nL_w(671)$, Chl-a, and SD for the season of (a–e) spring (March–May), (f–j) summer (June–August), (k–o) autumn (September–November), and (p–t) winter (December–February).

slightly to $\sim 0.3 \text{ mg m}^{-3}$ in the northern end region and spikes to over $\sim 1.0 \text{ mg m}^{-3}$ in the southern end region (Figs. 6g and 7b). Similarly, SD is quite stable at $\sim 22 \text{ m}$ for the majority of the transect line (typical oligotrophic waters) although decreased SD can be found in the coastal region of southern Lake Tahoe (Figs. 6h and 7b).

It is noted that significantly enhanced Chl-a and $nL_w(\lambda)$ and reduced SD are observed in the southern coast of the lake (Fig. 6), as well as in the southern end of the transect line (Fig. 7). In fact, VIIRS-derived $nL_w(\lambda)$ spectra in the southern coastal region show effects like typical bottom-affected water with significantly enhanced $nL_w(\lambda)$ spectra (Fig. 6). Although VIIRS-derived $nL_w(\lambda)$ spectra in the region might still be valid with the NIR-SWIR combined atmospheric algorithm (Wang and Shi, 2007), the lake bottom reflectance contributions to the enhancements of the derived $nL_w(\lambda)$ spectra in the visible bands (especially in the blue bands) can indeed lead to large errors in VIIRS-derived Chl-a and SD data in the southern end of the region. Thus, VIIRS-derived Chl-a and SD in the

bottom-impacted region may have significant errors and should not be considered valid.

3.4. Characterization of seasonal and interannual variability in water property

Seasonal variations of $nL_w(\lambda)$ spectra, Chl-a, and SD in Lake Tahoe are shown in Fig. 8. For $nL_w(443)$ (Fig. 8a, f, k, and p), it reaches its peak value in the summer season (Fig. 8f), and the minimum occurs in the winter season (Fig. 8p). The seasonal change of $nL_w(551)$ (Fig. 8b, g, l, and q) is relatively small (but quite noticeable) with highs in the summer and lows in the winter, corresponding well to the seasonal variation in SD (Fig. 8e, j, o, and t) (as expected). Similarly, the seasonal variation of $nL_w(671)$ in the lake is also very small (Fig. 8c, h, m, and r). Similar to the climatology results, spatial variations of Chl-a in the lake for each season are generally small (Fig. 8d, i, n, and s). The highest Chl-a value can

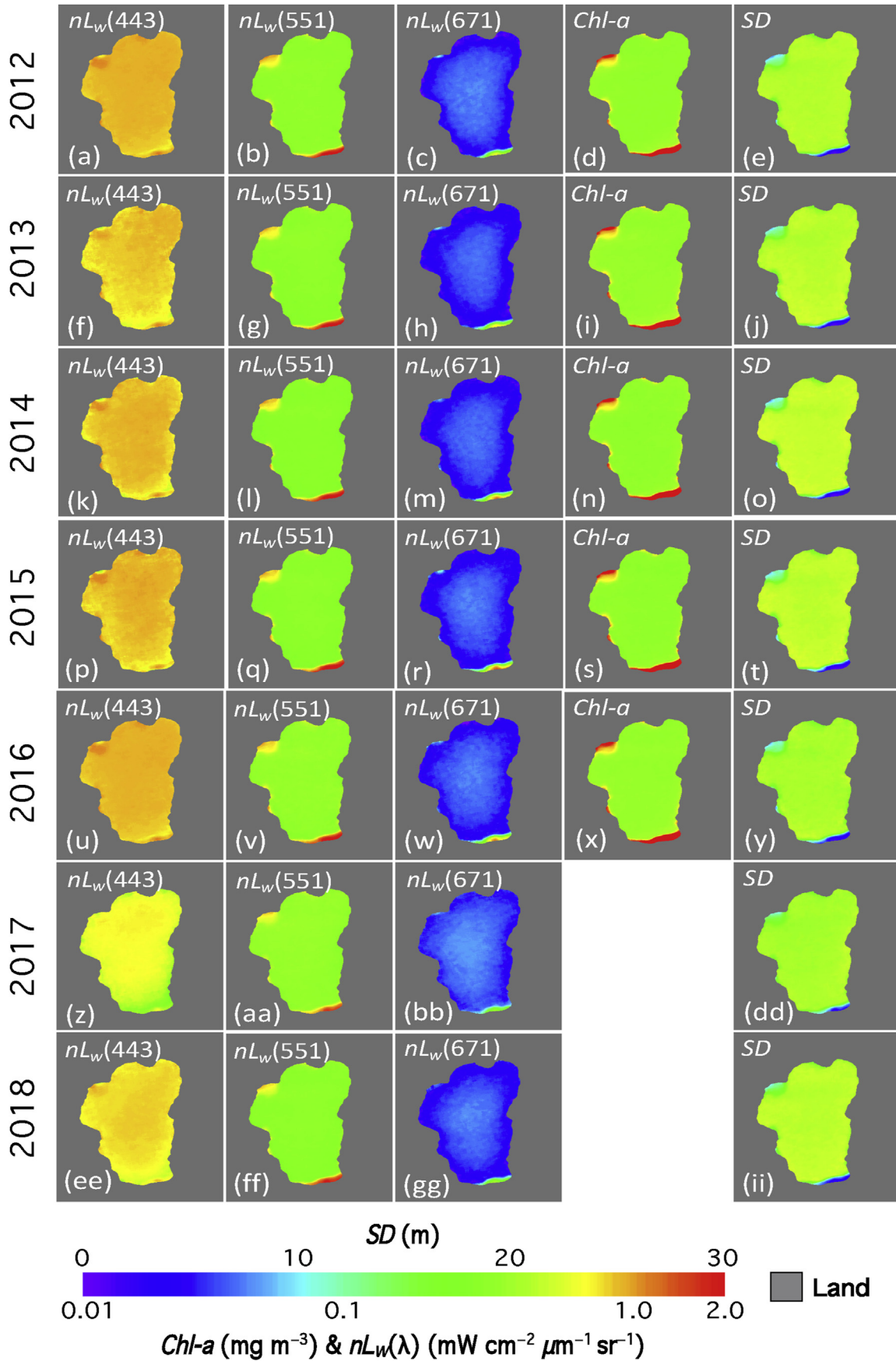


Fig. 9. VIIRS-derived interannual maps of water properties in Lake Tahoe for products of (along the row) $nL_w(443)$, $nL_w(551)$, $nL_w(671)$, $Chl-a$, and SD for the year of (a–e) 2012, (f–j) 2013, (k–o) 2014, (p–t) 2015, (u–y) 2016, (z–dd) 2017, and (ee–ii) 2018. Note that $Chl-a$ maps in 2017 and 2018 are not presented due to possible issue with the algorithm-caused overestimation.

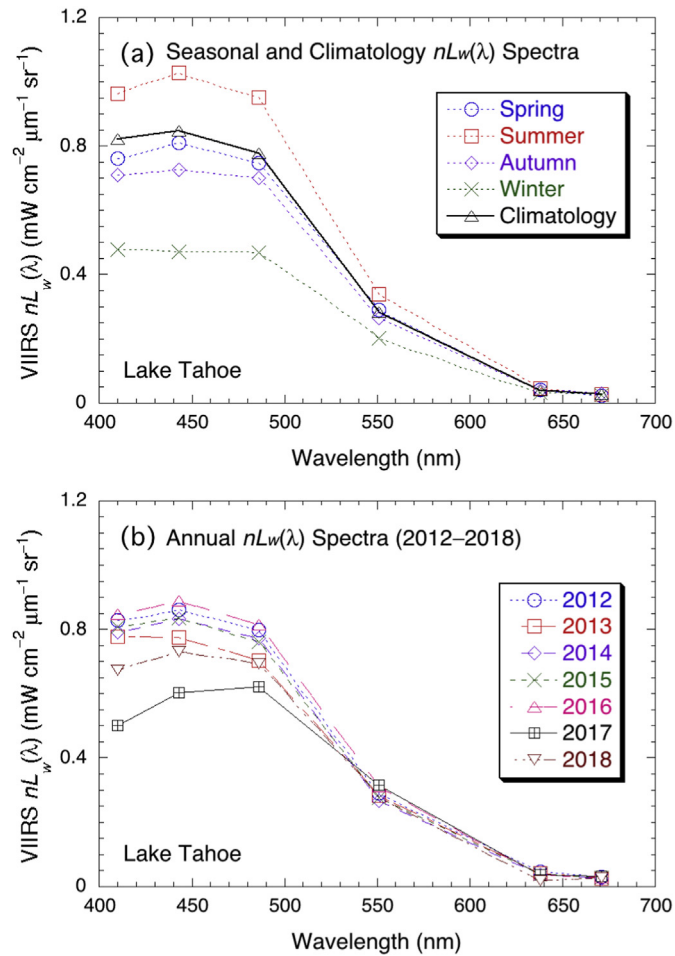


Fig. 10. VIIRS-derived $nL_w(\lambda)$ spectra in Lake Tahoe for (a) seasonal mean and climatology (2012–2016) and (b) annual mean in 2012–2018.

be found in the winter (Fig. 8s), while the lowest Chl-a occurs in the summer (Fig. 8i). The seasonal change of SD is also noticeable with the lowest SD in the summer (Fig. 8j) and the highest SD in the winter (Fig. 8t).

In addition, Fig. 9 shows the interannual variations of $nL_w(\lambda)$ spectra, Chl-a, and SD from 2012 to 2018. VIIRS-derived $nL_w(443)$ in 2017 (Fig. 9z) decreased remarkably as compared to the other years for the entire lake (Fig. 9a, f, k, p, u, and ee). Particularly, in the southern region of the lake, $nL_w(443)$ dropped to below $\sim 0.5 \text{ mW cm}^{-2} \mu\text{m}^{-1} \text{sr}^{-1}$. This indicates that there were increased amounts of absorbing components in the water column. It is noted that the statistical results in Fig. 9 should be quite reliable although there may be errors in the VIIRS-derived $nL_w(\lambda)$ spectra. Although $nL_w(443)$ increased in 2018 (Fig. 9ee), the values were still lower than those in the period of 2012–2016. Unlike $nL_w(443)$ (Fig. 9a, f, k, p, u, z, and ee), the interannual variations of $nL_w(551)$ (Fig. 9b, g, i, q, v, aa, and ff) and $nL_w(671)$ (Fig. 9c, h, m, r, w, bb, and gg) were not significant (not noticeable).

It is noted that VIIRS-derived Chl-a values in 2017 and 2018 may be over-estimated due to the Chl-a algorithm issue in dealing with the increased amount of inorganic suspended particles from high river runoff in that year. Thus, VIIRS-derived Chl-a values in 2017 and 2018 might be biased, and therefore, are not shown in Fig. 9. Except for the years 2017 and 2018, the spatial distributions of Chl-a in the other six years (Fig. 9d, i, n, s, and x) are similar. On the other hand, different from the Chl-a interannual variation, SD showed

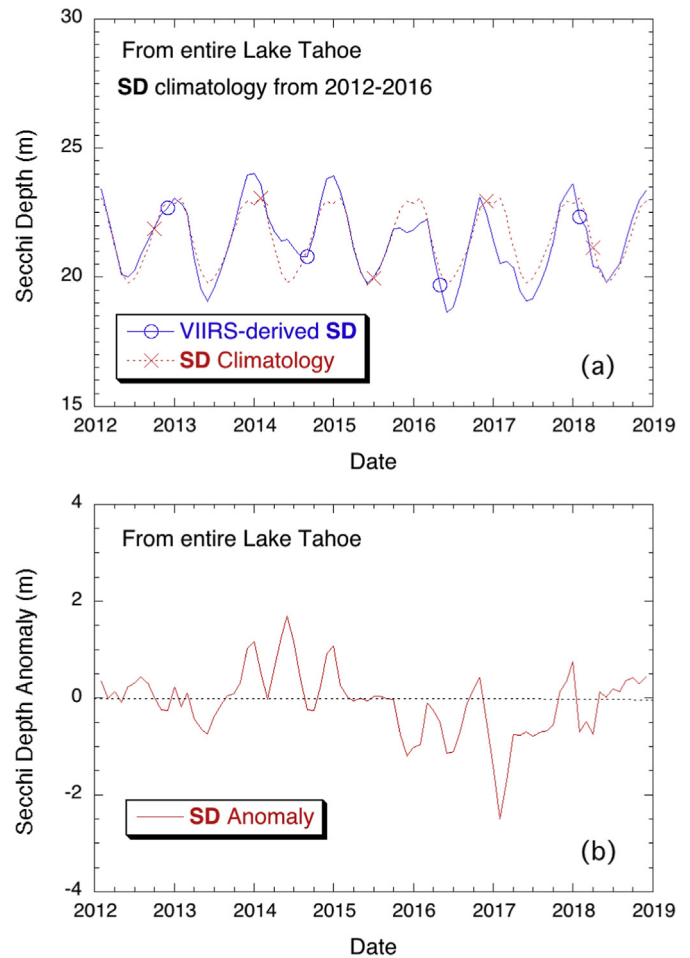


Fig. 11. VIIRS-derived temporal variation of the water property in Lake Tahoe between 2012 and 2018 for (a) SD and (b) SD anomaly. The red dotted line in plot (a) is the corresponding climatology monthly mean values derived from 2012 to 2016. (For interpretation of the references to color in this figure legend, the reader is referred to the Web version of this article.)

notable decreases in 2016 and 2017 (Fig. 9y and dd) in comparison to normal (climatology) SD values (Fig. 6h) and to those in the other years (Fig. 9e, j, o, t, and ii).

In addition, the seasonal and interannual variation in $nL_w(\lambda)$ spectra for the entire Lake Tahoe are quantitatively evaluated (Fig. 10). Fig. 10a shows the clear seasonal change in $nL_w(\lambda)$ spectra. Specifically, $nL_w(410)$, $nL_w(443)$, and $nL_w(486)$ values are the highest in the summer and the lowest in the winter. In the spring season, $nL_w(\lambda)$ spectrum is similar to the climatology (Fig. 10a). The seasonal differences in $nL_w(551)$ are smaller than those of the shorter wavebands, but are still obvious with highs in the summer and lows in the winter, reflecting the SD seasonal variation in the lake (Fig. 5b). It is noted again that $nL_w(638)$ and $nL_w(671)$ are both close to 0 for all four seasons.

The interannual variability of $nL_w(\lambda)$ spectra for Lake Tahoe is also significant (Fig. 10b). In particular, the $nL_w(\lambda)$ spectrum in 2017 was abnormal and outlying, showing significantly low values for $nL_w(410)$, $nL_w(443)$, and $nL_w(486)$. For example, $nL_w(410)$ in 2017 was $\sim 0.5 \text{ mW cm}^{-2} \mu\text{m}^{-1} \text{sr}^{-1}$, compared to the normal value of $\sim 0.8 \text{ mW cm}^{-2} \mu\text{m}^{-1} \text{sr}^{-1}$ in the other years. In 2018, the depression of $nL_w(410)$ was alleviated, but still lower than those in the other normal years. Fig. 10b shows that $nL_w(\lambda)$ spectra in 2012, 2014, 2015, and 2016 were all similar although some slight interannual variations did exist. All of these seasonal and interannual variations in

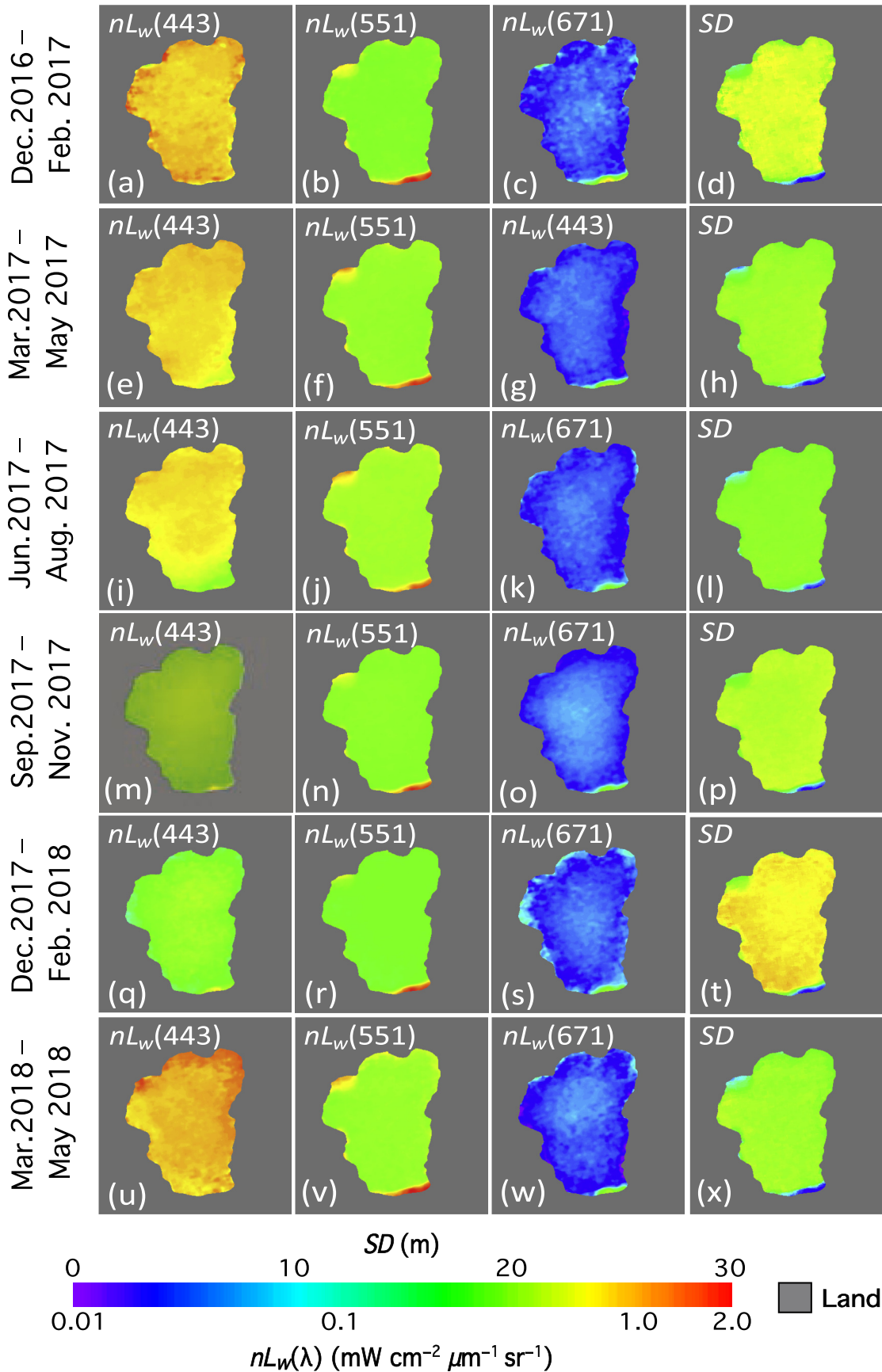


Fig. 12. VIIRS-derived Lake Tahoe water property of $nL_w(443)$, $nL_w(551)$, $nL_w(671)$, and SD (along the row) and for the 2017–2018 abnormal event with specific time period of (a–d) December 2016–February 2017, (e–h) March 2017–May 2017, (i–l) June 2017–August 2017, (m–p) September 2017–November 2017, (q–t) December 2017–February 2018, and (u–x) March 2018–May 2018.

VIIRS-derived $nL_w(\lambda)$ spectra are consistent with $nL_w(\lambda)$ spectral images as shown in Figs. 8 and 9.

3.5. The 2017–2018 anomaly event in Lake Tahoe

The interannual variability of water properties in Lake Tahoe in Figs. 9 and 10 shows that anomalous $nL_w(\lambda)$ spectra and SD occurred in 2017, and this abnormal event extended to 2018. Specifically, the median values of SD for the entire Lake Tahoe in each month between 2012 and 2018 were calculated to characterize and quantify the long-term temporal variations and the environmental anomaly in 2017.

The SD variation in Lake Tahoe between 2012 and 2018 is shown in Fig. 11a. The seasonal variation of SD was more pronounced in comparison to the interannual SD variation with SD ranging between 18–19 m and 23–24 m. The lowest SD values were in the summers of 2013, 2016, and 2017. After removing the seasonal SD variation, Fig. 11b shows that SD anomaly dropped below –2 m in the spring of 2017, and kept negative SD anomaly values for the entire 2017 year, consistent with the local media report (Staff-Report, 2018). In comparison, the negative SD anomaly values in 2013 and 2016 were mild and lasted only a couple of months. The temporal variation of the SD anomaly in Fig. 11b clearly shows that 2017 is the year with the least water clarity in the studying period between 2012 and 2018.

Fig. 12 provides the quantitative spatial image details of the temporal evolvments of $nL_w(\lambda)$ spectra and SD in the period from early 2017 to spring 2018. In the period between December 2016 and February 2017, all lake water properties (Fig. 12a–d) were similar to those of climatology for the winter season (Fig. 8p, q, r, and t). Starting in the spring of 2017 (March 2017–May 2017), the decreased $nL_w(443)$ (Fig. 12e) was found comparable to the typical $nL_w(443)$ in the same season (Fig. 8a). In the summer of 2017 (June 2017–August 2017), $nL_w(443)$ (Fig. 12i) was significantly lower than the same-season climatology $nL_w(443)$ (Fig. 8f). In the autumn of 2017, $nL_w(443)$ reached the lowest (Fig. 12m). It is also noted that SD in this season (Fig. 12p) was also lower than the SD climatology in the autumn (Fig. 8o).

Starting in the 2017–2018 winter season, $nL_w(\lambda)$ and SD went back to normal (Fig. 12q–t) although anomalous $nL_w(443)$ and SD were still remarkable in comparison to their typical values (Fig. 8p, q, r, and t). In the spring of 2018 (March 2018–May 2018), VIIRS-SNPP-measured $nL_w(\lambda)$ and SD (Fig. 12u–x) in the lake were fully recovered from the abnormal environmental event in 2017. Indeed, the lake's $nL_w(\lambda)$ and SD images in this period were similar to their typical ones (Fig. 8a, b, c, and e).

The water property anomaly in 2017 was observed also by the in situ water quality monitoring system and reported elsewhere (TERC, 2018). The annual average of SD (18.2 m) (TERC, 2018) was the lowest value ever recorded since Lake Tahoe long-term monitoring started in 1968, while the average SD in 2014, 2015, and 2016 in the lake were 23.7, 22.3, and 21.1 m, respectively. This anomalous environmental variation was attributed to the extreme weather and hydrologic events, all related to climatic change in the region. The total precipitation in the region was 175 cm in 2017 in comparison to amounts below 50 cm in 2014 and 2015. This high precipitation event led to high inflow carrying unusually high amount of sediments from surrounding tributaries. As a result, the concentrations of inorganic particles in the lake were elevated throughout the year, causing observed low water clarity, which is consistent with VIIRS-SNPP measurements.

The in situ Chl-a measurements did not show anomalous values in 2017, although the in situ Chl-a data exhibited relatively higher values in the winter. However, anomalous high Chl-a values were derived from VIIRS-SNPP measurements in 2017, which were

associated with low $nL_w(\lambda)$ in the shorter wavebands (410, 443, and 486 nm) (Figs. 9z and 10b) and may be heavily affected by absorption of high concentrations of inorganic sediments brought by high inflow as discussed above. This discrepancy (likely due to the satellite Chl-a algorithm issue), despite the reasonably good agreement of satellite-derived and in situ measurements in normal years, suggested the importance of improving the understanding of detailed properties of optically significant components in the water column and optical process of the lake for future biogeochemical monitoring with higher accuracy.

4. Discussions and conclusion

In the last three decades, satellite ocean color remote sensing (e.g., SeaWiFS, MODIS, VIIRS, etc.) has been widely used in user communities for scientific researches and applications (McClain, 2009) to understand global and regional water optical, biological, and biogeochemical properties, and to evaluate their impact on climatic change, natural hazards, and various other environmental variations. In fact, satellite ocean color data have been playing a critical role to monitor and understand water quality over the global open ocean, coastal, and inland waters (IOCCG, 2008; IOCCG, 2018).

The TOA Rayleigh scattering radiance computations, however, exhibited a significant error in satellite-measured global high-altitude water property data due to an issue in atmospheric correction to accurately account for the effects of the high-altitude water surface property (i.e., surface atmospheric pressure). The error resulted in considerably biased low $nL_w(\lambda)$ spectra which are often unusable for water property monitoring. Indeed, there are few satellite water color remote sensing studies over high-altitude lakes. It was shown that, with new improved Rayleigh radiance computations (Wang, 2016), satellite remote sensing can now routinely produce accurate and reliable water optical properties over high-altitude Lake Tahoe, similar to the well-established remote sensing capability over global sea-level inland bodies of water. The present results demonstrated that the new computation method can derive accurate $nL_w(\lambda)$ spectra from high-altitude inland waters. It also showed that Chl-a and SD values estimated from $nL_w(\lambda)$ spectra were reasonable. Therefore, satellite-measured $nL_w(\lambda)$ spectra, Chl-a, SD, and potentially other related products can be effectively used to characterize spatial and temporal variations of the lake water properties. This is indeed an important development for future satellite-based water quality monitoring of global inland waters.

Based on the in situ SD measurements, we developed a regional SD retrieval algorithm from VIIRS observations for Lake Tahoe. Chl-a and SD from VIIRS observations were generally consistent with the in situ measurements even though the algorithms are not perfect and some discrepancies indeed exist. It is also noted that $nL_w(671)$ is higher in the center of the lake as in Figs. 6, 8 and 9, while SD in the central lake is similar to SD in the coastal region. Although the differences are minor, e.g., $nL_w(671)$ values of 0.031, 0.036, and 0.031 $\text{mW cm}^{-2} \mu\text{m}^{-1} \text{sr}^{-1}$ for the transection line points of 5, 15, and 25 km in Fig. 7, respectively, it suggests that other water IOP components such as colored dissolved organic matter (CDOM), particularly suspended inorganic and organic particles may also contribute to the water property in the coastal region (reflected particularly in the SD measurements).

VIIRS-SNPP observations over Lake Tahoe between 2012 and 2018 are used to quantify water optical ($nL_w(\lambda)$ spectra), biological (Chl-a) and water quality (SD) properties in the lake. Climatology $nL_w(\lambda)$, Chl-a, and SD show that the spatial variation of the lake is quite small with Chl-a usually around -0.25 mg m^{-3} and enhanced $nL_w(\lambda)$ at the blue bands. The present results also showed that there

was seasonal variability in the measured variables. The highest Chl-a and SD normally occur in the winter season and the lowest values in the summer season. Significant seasonal $nL_w(\lambda)$ variations can also be found at the VIIRS spectral bands of 410, 443, and 486 nm. In the summer, VIIRS-derived $nL_w(\lambda)$ at these three bands are generally above $-0.8 \text{ mW cm}^{-2} \mu\text{m}^{-1} \text{ sr}^{-1}$, while they are normally below $-0.5 \text{ mW cm}^{-2} \mu\text{m}^{-1} \text{ sr}^{-1}$ in the winter. The seasonal variation for VIIRS-derived $nL_w(551)$ is also obvious with highs in the summer and lows in the winter.

In addition, there is significant interannual variability of water properties in Lake Tahoe observed from VIIRS measurements from 2012 to 2018. In particular, 2017 was an abnormal year with reduced SD and $nL_w(\lambda)$ at the blue bands. The anomaly started in the spring of 2017, reached the minimum for SD and $nL_w(443)$ in the 2017 summer-autumn season. During the 2017–2018 winter, SD started recovering, and went back to the normal in the spring of 2018. Anomalously low VIIRS-measured SD values were consistent with in situ measurements. Following the anomalous climate condition in the region during the 2017–2018 period, the increased suspended particles would probably be the cause of the low $nL_w(\lambda)$ in the blue end of the spectrum (Fig. 10b), which ultimately led to the overestimation of Chl-a in the season. This result suggests that a better understanding of optical processes of the lake with detailed information about optically active components in the water column is desired to account for such extreme conditions as well as future changes in environmental conditions. Still, the general trend of water clarity and Chl-a in a normal year were well estimated by VIIRS-SNPP observations with the current method.

The anomalous water properties observed from VIIRS-SNPP between 2017 and 2018 can be attributed to the interannual climate variability in the region. As an element of the tributary watershed drainage within the Truckee River Basin system, the Tahoe watershed covers more than 1000 km². Thus, the ecosystem can be significantly impacted by the precipitation variation in the region. In early 2017, the western U.S. including California and Nevada experienced a heavy precipitation period during the winter season following a multiyear drought period which impacted the region significantly (<https://www.ncdc.noaa.gov/sotc/national/201713>). Indeed, the total precipitation in the region was 175 cm in 2017 in comparison to below 50 cm in 2014 and 2015 (TERC, 2018). The anomalous precipitation amount and river runoff could transport more inorganic and organic suspended matters, CDOM, and nutrients to the lake, leading to the depressed SD in the 2017–2018 period.

The present research is the first study to derive, validate, and apply satellite-measured $nL_w(\lambda)$ spectra from high-altitude lakes using new Rayleigh radiance computations, and results shown here have important environmental and societal implications. The study demonstrates that satellite ocean color remote sensing can provide long-term monitoring with high frequency observations not only for the global ocean, coastal and sea-level inland waters, but also for global high-altitude inland waters. For example, lakes in the Tibetan Plateau, which can be considerably affected by the glacier melting due to global climate change, are rarely investigated, because they are remotely scattered around in a vast area, and usually have an inclement environment and weather conditions. Satellite remote sensing as demonstrated in this study can provide an effective and efficient tool to evaluate the long-term environmental variability of these systems in response to climate change.

Finally, it has been clearly shown that Lake Tahoe is generally a clear oligotrophic water body with high spatial uniformity over almost the entire lake. These characteristics make it ideal to be used as evaluation, validation, and a monitoring site for satellite ocean color remote sensing. In fact, Lake Tahoe has been used for calibration and validation of thermal bands for various satellite sensors

(Barsi et al., 2007; Hook et al., 2007; Steissberg et al., 2005; Tonooka and Palluconi, 2005; Tonooka et al., 2005). Advantages of Lake Tahoe as an additional calibration and validation site for satellite ocean color sensors include (1) logistically easy to access for maintaining the site (as the site has already been established and used for calibration and validation for thermal bands), (2) located at high-altitude (~2 km) with less atmospheric effects (i.e., less TOA radiance contributions from molecules and aerosols), and (3) weather conditions are generally cooperative (e.g., no hurricanes) and instruments at the location are more controllable. Therefore, Lake Tahoe can potentially serve as a good calibration and validation site for satellite-derived ocean/water property products.

Declaration of competing interest

The authors declare that they have no known competing financial interests or personal relationships that could have appeared to influence the work reported in this paper.

Acknowledgments

This research was supported by the Joint Polar Satellite System (JPSS) funding. We thank two anonymous reviewers for their useful comments. The views, opinions, and findings contained in this paper are those of the authors and should not be construed as an official NOAA or U.S. Government position, policy, or decision.

References

- Barnes, B.B., Cannizzaro, J.P., English, D.C., Hu, C., 2019. Validation of VIIRS and MODIS reflectance data in coastal and oceanic waters: an assessment of methods. *Remote Sens. Environ.* 220, 110–123.
- Barsi, J.A., Hook, S.J., Schott, J.R., Raqueno, N.G., Markham, B.L., 2007. Landsat-5 thematic mapper thermal band calibration update. *Geosci. Rem. Sens. Lett. IEEE* 4, 552–555.
- Binding, C., Jerome, J., Bukata, R., Booty, W., 2008. Spectral absorption properties of dissolved and particulate matter in Lake Erie. *Remote Sens. Environ.* 112, 1702–1711.
- Binding, C.E., Greenberg, T.A., Watson, S.B., Rastin, S., Gould, J., 2015. Long term water clarity changes in North America's Great Lakes from multi-sensor satellite observations. *Limnol. Oceanogr.* 60, 1976–1995.
- Bolgrien, D.W., Brooks, A.S., 1992. Analysis of thermal features of Lake Michigan from AVHRR satellite images. *J. Great Lake. Res.* 18, 259–266.
- Bulgarelli, B., Kiselev, V., Zibordi, G., 2017. Adjacency effects in satellite radiometric products from coastal waters: a theoretical analysis for the northern Adriatic Sea. *Appl. Optic.* 56, 854–869.
- Chang, C.C.Y., Kuwabara, J.S., Pasilis, S.P., 1992. Phosphate and iron limitation of phytoplankton biomass in Lake Tahoe. *Can. J. Fish. Aquat. Sci.* 49, 1206–1215.
- Clark, D.K., Gordon, H.R., Voss, K.J., Ge, Y., Broenkow, W., Trees, C., 1997. Validation of atmospheric correction over the ocean. *J. Geophys. Res.* 102, 17209–17217.
- Coats, R., Perez-Losada, J., Schladow, G., Richards, R.C., Goldman, C.R., 2006. The warming of lake Tahoe. *Climatic Change* 76, 121–148.
- Dolislager, L.J., VanCuren, R., Pederson, J.R., Lashgari, A., McCauley, E., 2012. A summary of the Lake Tahoe atmospheric deposition study (LTADS). *Atmos. Environ.* 46, 618–630.
- Goldberg, M.D., Kilcoyne, H., Cikanek, H., Mehta, A., 2013. Joint Polar Satellite System: the United States next generation civilian polar-orbiting environmental satellite system. *J. Geophys. Res. Atmos.* 118, 13463–13475. <https://doi.org/10.1002/2013jd020389>.
- Goldman, C.R., 2000. Four decades of change in two subalpine lakes. *Verh. Int. Ver. Limnol.* 27, 7–26.
- Gordon, H.R., 2005. Normalized water-leaving radiance: revisiting the influence of surface roughness. *Appl. Optic.* 44, 241–248.
- Gordon, H.R., Brown, J.W., Evans, R.H., 1988a. Exact Rayleigh scattering calculations for use with the nimbus-7 coastal zone color scanner. *Appl. Optic.* 27, 862–871.
- Gordon, H.R., Brown, O.B., Evans, R.H., Brown, J.W., Smith, R.C., Baker, K.S., Clark, D.K., 1988b. A semi-analytic radiance model of ocean color. *J. Geophys. Res.* 93, 10909–10924.
- Gordon, H.R., Wang, M., 1994. Retrieval of water-leaving radiance and aerosol optical thickness over the oceans with SeaWiFS: a preliminary algorithm. *Appl. Optic.* 33, 443–452.
- Hlaing, S., Harmel, T., Gilerson, A., Foster, R., Weidemann, A., Arnone, R., Wang, M., Ahmed, S., 2013. Evaluation of the VIIRS ocean color monitoring performance in coastal regions. *Remote Sens. Environ.* 139, 398–414.
- Hook, S.J., Chandler, G., Barsi, J.A., Alley, R.E., Abtahi, A., Palluconi, F.D., Markham, B.L., Richards, R.C., Schladow, S.G., Helder, D.L., 2004. In-flight validation and

- recovery of water surface temperature with Landsat 5 thermal infrared data using an automated high altitude lake validation site at Lake Tahoe CA/NV, USA. *IEEE Trans. Geosci. Rem. Sens.* 42, 2767–2776.
- Hook, S.J., Vaughan, R.G., Tonooka, H., Schladow, S.G., 2007. Absolute radiometric in-flight validation of mid infrared and thermal infrared data from ASTER and MODIS on the Terra spacecraft using the Lake Tahoe, CA/NA, USA, automated validation site. *IEEE Trans. Geosci. Rem. Sens.* 45, 1798–1807.
- Hu, C., 2009. A novel ocean color index to detect floating algae in the global oceans. *Remote Sens. Environ.* 113, 2118–2129.
- Hu, C., Barnes, B.B., Feng, L., Wang, M., Jiang, L., 2020. On the trade space between ocean color data quality and data quantity: impacts of quality control flags. *Geosci. Rem. Sens. Lett. IEEE* 16. <https://doi.org/10.1109/lgrs.2019.2936220>.
- Hu, C., Lee, Z., Franz, B.A., 2012. Chlorophyll a algorithms for oligotrophic oceans: a novel approach based on three-band reflectance difference. *J. Geophys. Res.* 117, C01011. <https://doi.org/10.1029/2011jc007395>.
- Hu, C., Lee, Z., Ma, R., Yu, K., Li, D., Shang, S., 2010. Moderate resolution imaging spectroradiometer (MODIS) observations of cyanobacteria blooms in Taihu lake, China. *J. Geophys. Res.* 115, C04002. <https://doi.org/10.1029/2009jc005511>.
- IOCCG, 2008. Why ocean colour? The societal benefits of ocean-colour technology. In: Platt, T., Hoepffner, N., Stuart, V., Brown, C. (Eds.), Reports of the International Ocean-Colour Coordinating Group. IOCCG, Dartmouth, Canada. <https://dx.doi.org/10.25607/OBP-97>.
- IOCCG, 2010. Atmospheric correction for remotely-sensed ocean-colour products. In: Wang, M. (Ed.), Reports of the International Ocean-Colour Coordinating Group. IOCCG, Dartmouth, Canada. <https://dx.doi.org/10.25607/OBP-101>.
- IOCCG, 2018. Earth observations in support of global water quality monitoring. In: Greb, S., Dekker, A., Binding, C. (Eds.), Reports of the International Ocean-Colour Coordinating Group. IOCCG, Dartmouth, Canada. <https://dx.doi.org/10.25607/OBP-113>.
- Jassby, A.D., Goldman, C.R., Reuter, J.E., Richards, R.C., 1999. Origins and scale dependence of temporal variability in the transparency of Lake Tahoe, California-Nevada. *Limnol. Oceanogr.* 44, 282–294.
- Jassby, A.D., Reuter, J.E., Axler, R.P., Goldman, C.R., Hackley, S.H., 1994. Atmospheric deposition of nitrogen and phosphorus in the annual nutrient load of Lake Tahoe (California Nevada). *Water Resour. Res.* 30.
- Jassby, A.D., Reuter, J.E., Goldman, C.R., 2003. Determining long-term water quality change in the presence of climate variability: lake Tahoe (USA). *Can. J. Fish. Aquat. Sci.* 60.
- Jiang, L., Wang, M., 2013. Identification of pixels with stray light and cloud shadow contaminations in the satellite ocean color data processing. *Appl. Optic.* 52, 6757–6770.
- Jiang, L., Wang, M., 2014. Improved near-infrared ocean reflectance correction algorithm for satellite ocean color data processing. *Optic Express* 22, 21657–21678.
- Knaeps, E., Ruddick, K., Doxaran, D., Dogliotti, A., Nechad, B., Raymaekers, D., Sterckx, S., 2015. A SWIR based algorithm to retrieve total suspended matter in extremely turbid waters. *Remote Sens. Environ.* 168, 66–79.
- Lee, Z.P., Carder, K.L., Arnone, R.A., 2002. Deriving inherent optical properties from water color: a multiple quasi-analytical algorithm for optically deep waters. *Appl. Optic.* 41, 5755–5772.
- Lee, Z.P., Darecki, M., Carder, K., Davis, C., Stramski, D., Rhea, W., 2005. Diffuse attenuation coefficient of downwelling irradiance: an evaluation of remote sensing methods. *J. Geophys. Res.* 110, C02017. <https://doi.org/10.1029/2004JC002573>.
- Lee, Z.P., Shang, S., Qi, L., Yan, J., Lin, G., 2016. A semi-analytical scheme to estimate Secchi-disk depth from Landsat-8 measurements. *Remote Sens. Environ.* 177, 101–106.
- Mackey, K.R.M., Hunter, D., Fischer, E.V., Jiang, Y.L., Allen, B., Chen, Y., Liston, A., Reuter, J.E., Schladow, G., Paytan, A., 2013. Aerosol-nutrient-induced picoplankton growth in Lake Tahoe. *J. Geophys. Res. Biogeosci.* 118, 1054–1067.
- McClain, C.R., 2009. A decade of satellite ocean color observations. *Annu. Rev. Mar. Sci.* 1, 19–42.
- Mikelsons, K., Wang, M., Jiang, L., 2020. Statistical evaluation of satellite ocean color data retrievals. *Remote Sens. Environ.* 237, 111601. <https://doi.org/10.1016/j.rse.2019.111601>.
- Morel, A., Gentili, G., 1996. Diffuse reflectance of oceanic waters. III. Implication of bidirectionality for the remote-sensing problem. *Appl. Optic.* 35, 4850–4862.
- Morel, A., Maritorena, S., 2001. Bio-optical properties of oceanic waters: a reappraisal. *J. Geophys. Res.* 106, 7163–7180.
- Nechad, B., Ruddick, K., Park, Y., 2010. Calibration and validation of a generic multisensor algorithm for mapping of total suspended matter in turbid waters. *Remote Sens. Environ.* 114, 854–866.
- O'Reilly, J.E., Maritorena, S., Mitchell, B.G., Siegel, D.A., Carder, K.L., Garver, S.A., Kahru, M., McClain, C.R., 1998. Ocean color chlorophyll algorithms for SeaWiFS. *J. Geophys. Res.* 103, 24937–24953.
- O'Reilly, J.E., Werdell, P.J., 2019. Chlorophyll algorithms for ocean color sensors - OC4, OC5 & OC6. *Remote Sens. Environ.* 229, 32–47.
- Parada, R.J., Thome, K.J., Santer, R.P., 1997. Results of dark target vicarious calibration using Lake Tahoe. *Proc. SPIE* 2957, 332–343. <https://doi.org/10.1117/12.265452>.
- Ramachandran, S., Wang, M., 2011. Near-real-time ocean color data processing using ancillary data from the Global Forecast System model. *IEEE Trans. Geosci. Rem. Sens.* 49, 1485–1495.
- Rose, K.C., Williamson, C.E., Schladow, S.G., Winder, M., Oris, J.T., 2009. Patterns of spatial and temporal variability of UV transparency in Lake Tahoe, California-Nevada. *J. Geophys. Res. Biogeosci.* 114, G00D03. <https://doi.org/10.1029/2008JG000816>.
- Sahoo, G.B., Forrest, A.L., Schladow, S.G., Reuter, J.E., Coats, R., Dettinger, M., 2016. Climate change impacts on lake thermal dynamics and ecosystem vulnerabilities. *Limnol. Oceanogr.* 61, 496–507.
- Sahoo, G.B., Schladow, S.G., Reuter, J.E., 2010. Effect of sediment and nutrient loading on Lake Tahoe optical conditions and restoration opportunities using a newly developed lake clarity model. *Water Resour. Res.* 46, W10505. <https://doi.org/10.1029/2009WR008447>.
- Shi, W., Wang, M., 2015. Decadal changes of water properties in the Aral Sea observed by MODIS-Aqua. *J. Geophys. Res. Oceans* 120, 4687–4708. <https://doi.org/10.1002/2015JC010937>.
- Shi, W., Wang, M., 2019. A blended inherent optical property algorithm for global satellite ocean color observations. *Limnol Oceanogr. Methods* 17, 377–394.
- Shi, W., Wang, M., Zhang, Y., 2019. Inherent optical properties in Lake Taihu derived from VIIRS satellite observations. *Rem. Sens.* 11, 1426. <https://doi.org/10.3390/rs11121426>.
- Shi, W., Zhang, Y., Wang, M., 2018. Deriving total suspended matter concentration from the near-infrared-based inherent optical properties over turbid waters: a case study in Lake Taihu. *Rem. Sens.* 10, 333. <https://doi.org/10.3390/rs10020333>.
- Smith, R.C., Tyler, J.E., Goldman, C.R., 1973. Optical properties and color of lake Tahoe and Crater Lake. *Limnol. Oceanogr.* 18, 189–199.
- Son, S., Wang, M., 2019. VIIRS-derived water turbidity in the Great Lakes. *Rem. Sens.* 11, 1448. <https://doi.org/10.3390/rs11121448>.
- Staff-Report, 2018. Lake Tahoe Clarity Decreased 9.5 Feet in 2017. Tahoe Daily Tribune. <https://www.tahoe-daily-tribune.com/news/local/lake-tahoe-clarity-decreased-9-5-feet-in-2017/>.
- Steissberg, T.E., Hook, S.J., Schladow, S.G., 2005. Characterizing partial upwellings and surface circulation at Lake Tahoe, California-Nevada, USA with thermal infrared images. *Remote Sens. Environ.* 99, 2–15.
- TERC, 2018. Tahoe: State of the Lake Report 2018. University of California, Davis. <https://tahoe.ucdavis.edu>.
- Thome, K.J., Arai, K., Hook, S., Kieffer, H., Lang, H., Matsunaga, T., Ono, A., Palluconi, F., Sakuma, H., Slater, P., Takashima, T., Tonooka, H., Tsuchida, S., Welch, R.M., Zalewski, E., 1998. ASTER preflight and in-flight calibration and the validation of level 2 products. *IEEE Trans. Geosci. Rem. Sens.* 36, 1161–1172.
- Thuillier, G., Herse, M., Labs, D., Foujols, T., Peetermans, W., Gillotay, D., Simon, P.C., Mandel, H., 2003. The solar spectral irradiance from 200 to 2400 nm as measured by the SOLSPEC spectrometer from the ATLAS and EURECA missions. *Sol. Phys.* 214, 1–22.
- Tonooka, H., Palluconi, F.D., 2005. Validation of ASTER/TIR standard atmospheric correction using water surfaces. *IEEE Trans. Geosci. Rem. Sens.* 43, 2769–2777.
- Tonooka, H., Palluconi, F.D., Hook, S.J., Matsunaga, T., 2005. Vicarious calibration of ASTER thermal infrared bands. *IEEE Trans. Geosci. Rem. Sens.* 43, 2733–2746.
- Wang, M., 1999. A sensitivity study of SeaWiFS atmospheric correction algorithm: effects of spectral band variations. *Remote Sens. Environ.* 67, 348–359.
- Wang, M., 2002. The Rayleigh lookup tables for the SeaWiFS data processing: accounting for the effects of ocean surface roughness. *Int. J. Rem. Sens.* 23, 2693–2702.
- Wang, M., 2005. A refinement for the Rayleigh radiance computation with variation of the atmospheric pressure. *Int. J. Rem. Sens.* 26, 5651–5663.
- Wang, M., 2006. Effects of ocean surface reflectance variation with solar elevation on normalized water-leaving radiance. *Appl. Optic.* 45, 4122–4128.
- Wang, M., 2007. Remote sensing of the ocean contributions from ultraviolet to near-infrared using the shortwave infrared bands: simulations. *Appl. Optic.* 46, 1535–1547.
- Wang, M., 2016. Rayleigh radiance computations for satellite remote sensing: accounting for the effect of sensor spectral response function. *Optic Express* 24, 12414–12429.
- Wang, M., Isaacman, A., Franz, B.A., McClain, C.R., 2002. Ocean color optical property data derived from the Japanese ocean color and temperature scanner and the French polarization and directionality of the Earth's reflectances: a comparison study. *Appl. Optic.* 41, 974–990.
- Wang, M., Jiang, L., 2018a. Atmospheric correction using the information from the short blue band. *IEEE Trans. Geosci. Rem. Sens.* 56, 6224–6237. <https://doi.org/10.1109/tgrs.2018.2833839>.
- Wang, M., Jiang, L., 2018b. VIIRS-derived ocean color product using the imaging bands. *Remote Sens. Environ.* 206, 275–286.
- Wang, M., Jiang, L., Liu, X., Son, S., Sun, J., Shi, W., Tan, L., Mikelsons, K., Wang, X., Lance, V., 2016a. VIIRS ocean color products: a progress update. In: Proc. the IEEE Int. Geosci. Remote Sens. Symposium (IGARSS). <https://doi.org/10.1109/IGARSS.2016.7730528>, 5848–5851, Beijing, China, July 5810–5815.
- Wang, M., Liu, X., Tan, L., Jiang, L., Son, S., Shi, W., Rausch, K., Voss, K., 2013. Impact of VIIRS SDR performance on ocean color products. *J. Geophys. Res. Atmos.* 118, 10347–10360. <https://doi.org/10.1002/jgrd.50793>.
- Wang, M., Nim, C.J., Son, S., Shi, W., 2012a. Characterization of turbidity in Florida's Lake Okeechobee and Caloosahatchee and St. Lucie estuaries using MODIS-Aqua measurements. *Water Res.* 46, 5410–5422.
- Wang, M., Shi, W., 2005. Estimation of ocean contribution at the MODIS near-infrared wavelengths along the east coast of the U.S.: two case studies. *Geophys. Res. Lett.* 32, L13606. <https://doi.org/10.1029/2005GL022917>.
- Wang, M., Shi, W., 2006. Cloud masking for ocean color data processing in the coastal regions. *IEEE Trans. Geosci. Rem. Sens.* 44, 3196–3205.
- Wang, M., Shi, W., 2007. The NIR-SWIR combined atmospheric correction approach for MODIS ocean color data processing. *Optic Express* 15, 15722–15733.

- Wang, M., Shi, W., Jiang, L., 2012b. Atmospheric correction using near-infrared bands for satellite ocean color data processing in the turbid western Pacific region. *Optic Express* 20, 741–753.
- Wang, M., Shi, W., Jiang, L., Liu, X., Son, S., Voss, K., 2015. Technique for monitoring performance of VIIRS reflective solar bands for ocean color data processing. *Optic Express* 23, 14446–14460.
- Wang, M., Shi, W., Jiang, L., Voss, K., 2016b. NIR- and SWIR-based on-orbit vicarious calibrations for satellite ocean color sensors. *Optic Express* 24, 20437–20453.
- Wang, M., Shi, W., Tang, J., 2011. Water property monitoring and assessment for China's inland Lake Taihu from MODIS-Aqua measurements. *Remote Sens. Environ.* 115, 841–854.
- Wang, M., Son, S., 2016. VIIRS-derived chlorophyll-a using the ocean color index method. *Remote Sens. Environ.* 182, 141–149.
- Wang, M., Son, S., Harding Jr., L.W., 2009a. Retrieval of diffuse attenuation coefficient in the Chesapeake Bay and turbid ocean regions for satellite ocean color applications. *J. Geophys. Res.* 114, C10011. <https://doi.org/10.1029/2009JC005286>.
- Wang, M., Son, S., Shi, W., 2009b. Evaluation of MODIS SWIR and NIR-SWIR atmospheric correction algorithm using SeaBASS data. *Remote Sens. Environ.* 113, 635–644.
- Watanabe, S., Vincent, W.F., Reuter, J., Hook, S.J., Schladow, S.G., 2016. A quantitative blueness index for oligotrophic waters: application to Lake Tahoe, California-Nevada. *Limnol Oceanogr. Methods* 14, 100–109.
- Wei, J., Lee, Z., Shang, S., 2016. A system to measure the data quality of spectral remote-sensing reflectance of aquatic environments. *J. Geophys. Res. Oceans* 121, 8189–8207. <https://doi.org/10.1002/2016JC012126>.
- Werdell, P.J., Franz, B.A., Bailey, S.W., Feldman, G.C., Boss, E., Brando, V.E., Dowell, M., Hirata, T., Lavender, S.J., Lee, Z.P., Loisel, H., Maritorena, S., Melin, F., Moore, T.S., Smyth, T.J., Antoine, D., Devred, E., d'Andon, O.H.F., Mangin, A., 2013. Generalized ocean color inversion model for retrieving marine inherent optical properties. *Appl. Optic.* 52, 2019–2037.
- Yang, H., Gordon, H.R., 1997. Remote sensing of ocean color: assessment of water-leaving radiance bidirectional effects on atmospheric diffuse transmittance. *Appl. Optic.* 36, 7887–7897.
- Yu, X., Lee, Z., Shen, F., Wang, M., Wei, J., Jiang, L., Shang, Z., 2019. An empirical algorithm to seamlessly retrieve the concentration of suspended particulate matter from water color across ocean to turbid river mouths. *Remote Sens. Environ.* 235, 111491. <https://doi.org/10.1016/j.rse.2019.111491>.